Effective resonant model and simulations in the time-domain of wave scattering from a periodic row of highly-contrasted inclusions

Marie Touboul, Kim Pham, Agnès Maurel, Jean-Jacques Marigo, Bruno Lombard, Cédric Bellis

Effective resonant model and simulations in the time-domain of wave scattering from a periodic row of highly-contrasted inclusions

Marie Touboul[a], Kim Pham[b,*], Agnès Maurel[c],
Jean-Jacques Marigo[d], Bruno Lombard[a], Cédric Bellis[a]

[a]*Aix Marseille Univ, CNRS, Centrale Marseille, LMA UMR 7031, Marseille, France*
[b]*IMSIA, CNRS, ENSTA ParisTech, 828 Bd des Maréchaux, 91732 Palaiseau, France*
[c]*Institut Langevin, CNRS, ESPCI ParisTech, 1 rue Jussieu, 75005 Paris, France*
[d]*Laboratoire de Mécanique des Solides, CNRS, Ecole Polytechnique, 91120 Palaiseau, France*

Abstract

The time-domain propagation of scalar waves across a periodic row of inclusions is considered in 2D. As the typical wavelength within the background medium is assumed to be much larger than the spacing between inclusions and the row width, the physical configuration considered is in the low-frequency homogenization regime. Furthermore, a high contrast between one of the constitutive moduli of the inclusions and of the background medium is also assumed. So the wavelength within the inclusions is of the order of their typical size, which can further induce local resonances within the microstructure. In Pham et al. (2017), two-scale homogenization techniques and matched-asymptotic expansions have been employed to derive, in the harmonic regime, effective jump conditions on an equivalent interface. This homogenized model is frequency-dependent due to the resonant behavior of the inclusions. In this context, the present article aims at investigating, directly in the time-domain, the scattering of waves by such a periodic row of resonant scatterers. Its effective behavior is first derived in the time-domain and some energy properties of the resulting homogenized model are analyzed. Time-domain numerical simulations are then performed to illustrate the main features of the effective interface model obtained and to assess its relevance in comparison with full-field simulations.

Keywords: dynamic homogenization, resonant media, matched asymptotic expansions

1. Introduction

Let us consider a microstructured medium composed of inclusions periodically embedded in a background medium, or matrix, and submitted to a dynamical excitation. When the characteristic wavelength within the matrix is much larger than the period length, the microstructure can be advantageously replaced, at the macro-scale, by a homogeneous effective medium. To do so, homogenization methods Bensoussan et al. (2011); Sanchez-Hubert and Sanchez-Palencia (1992) can be employed to derive the properties of the sought effective medium. When the heterogeneities amount to a periodic row of inclusions (see Figure 1), then homogenization techniques and matched-asymptotic expansions can be deployed to obtain effective jump conditions on an equivalent interface, see Marigo and Maurel (2016); Marigo and Pideri (2011); Delourme (2010); David et al. (2012); Marigo et al. (2017); Bonnet-Bendhia et al. (2004). Furthermore, from energy-based considerations, its has been shown that an equivalent interface of non-zero width ensures the stability of the resulting model, while no field

*Corresponding author. E-mail address: touboul@lma.cnrs-mrs.fr

remains defined within the enlarged region. As a result, wave propagation across the microstructured row of inclusions is modeled, in the long-wavelength regime, using effective jump conditions on both sides of an enlarged interface.

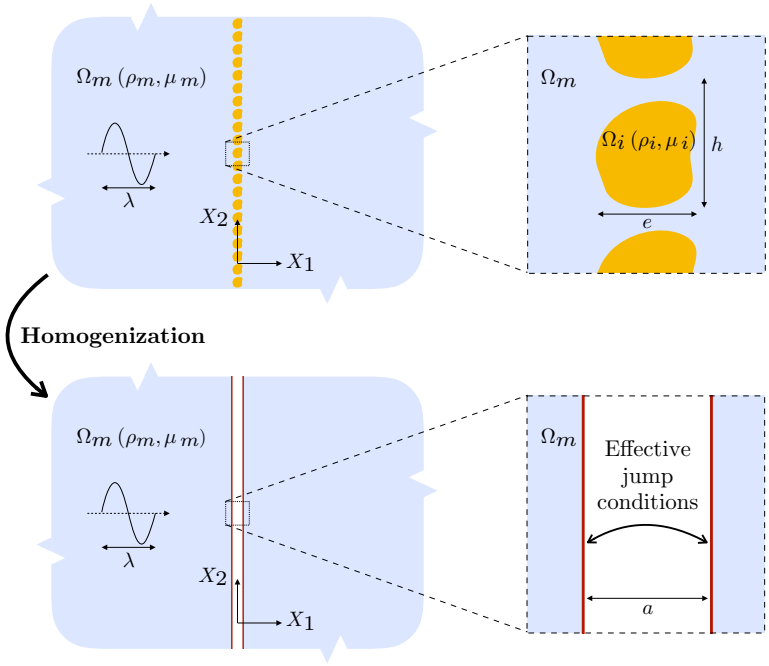

Figure 1: Homogenization process in the case of a single periodic row of inclusions.

For a periodic row of elastic inclusions, effective jump conditions have been derived in Marigo et al. (2017) in the case where the constitutive moduli of the inclusions and of the matrix are of the same order of magnitude. Nevertheless, when there is a high parameter contrast between the inclusions and the matrix then a specific homogenized model has to be formulated. Such a configuration is particularly relevant in the context of the metamaterials that are generally designed to exhibit specific effective behaviors, the control of waves being one application of interest in the dynamical context considered here. For microstructures characterized by high material contrasts then internal resonances can occur, a phenomenon which can be used in turn at the macroscopic level to drive the behavior of waves that propagate through them. As an example, resonant meta-surfaces have been designed to maximize sound absorption, see Ma et al. (2014); Schwan et al. (2017); Maurel et al. (2019a). The homogenization of a periodic row of highly-contrasted inclusions has been investigated theoretically in Pham et al. (2017) in the harmonic regime. This analysis leads to the construction of an equivalent enlarged interface on which a set of effective jump conditions applies. However, unlike the non-resonant case, the effective parameters of these conditions turn out to be frequency-dependent due to the local resonances that can occur within the microstructure.

The present paper focuses on the propagation of waves across a periodic row of highly-contrasted inclusions. The homogenization of such a resonant microstructure is specifically conducted in the transient regime. Effective properties are derived in the time domain in Section 2 and the resulting model is analyzed using energy-based arguments. In particular, a condition on the thickness of the enlarged interface is obtained to ensure the conservation of an energy. Section 3 aims at both illustrating the effective dynamical behavior obtained and at validating the effective model through comparisons with full-field, i.e. microstructure-based, simulations. One notes that the time-domain simulations

presented here rely on the numerical method introduced in Touboul et al. (2020) to handle resonant jump conditions on meta-interfaces. Numerical results are discussed to highlight the computational merits of the homogenized model for the configuration of interest compared to full-field simulations. Results confirm a good agreement between full-field and homogenized simulations as the wavelength decreases towards the characteristic size of the inclusions.

2. Homogenized resonant model in the time domain

Let us consider the propagation of *scalar* waves in 2D across a periodic row of inclusions $\cup_i \Omega_i$ embedded within a homogeneous matrix Ω_m, with both media being assumed to be isotropic. The thickness and the periodicity of the row are denoted by e and h, respectively and we assume that $e = \mathcal{O}(h)$. The time and the spatial coordinates are denoted by t and $\boldsymbol{X} = (X_1, X_2)$, respectively, with X_2 being the direction of periodicity of the inclusions as shown in Figure 1. The microstructured medium is characterized by two constitutive moduli, the mass density ρ and the shear modulus μ, that are piecewise constant:

$$(\rho, \mu)(\boldsymbol{X}) = \begin{cases} (\rho_m, \mu_m) & \text{in the matrix,} \\ (\rho_i, \mu_i) & \text{in the inclusions.} \end{cases}$$

The problem is considered within the framework of the linear anti-plane elasticity model. The time-domain governing equation for the scalar out-of-plane displacement U writes:

$$\operatorname{div}\big(\mu(\boldsymbol{X})\boldsymbol{\nabla} U(\boldsymbol{X}, t)\big) = \rho(\boldsymbol{X})\frac{\partial^2 U}{\partial t^2}(\boldsymbol{X}, t).$$

Introducing the scalar velocity field $V = \partial U/\partial t$, this system can be rewritten as a first-order system in time for V and for the stress vector $\boldsymbol{\Sigma} = (\Sigma_1, \Sigma_2)^T$:

$$\begin{cases} \dfrac{\partial \boldsymbol{\Sigma}}{\partial t}(\boldsymbol{X}, t) = \mu \boldsymbol{\nabla} V(\boldsymbol{X}, t), \\ \rho \dfrac{\partial V}{\partial t}(\boldsymbol{X}, t) = \operatorname{div} \boldsymbol{\Sigma}(\boldsymbol{X}, t), \end{cases} \tag{1}$$

with V and $\boldsymbol{\Sigma} \cdot \boldsymbol{n}$ being continuous at each matrix/inclusion interface $\partial\Omega_i$, given that $\boldsymbol{n}$ is the *inward* unit normal on each $\partial\Omega_i$. The system (1) is also relevant to other physical configurations, such as acoustic waves for which the fields $\boldsymbol{\Sigma}$, V, ρ and $1/\mu$ would stand instead for velocity, pressure, compressibility and mass density, respectively.

Considering an illumination by an incident wave or external sources, a characteristic wavelength λ within the matrix is assumed to be much larger than the spacing h between successive inclusions. Defining the wavenumber within the matrix as $k_m = 2\pi/\lambda$, we introduce the ratio $\eta = k_m h$ that satisfies $\eta \ll 1$ for the configurations of interest. This geometrical assumption allows to homogenize the microstructure in the long-wavelength regime. The choice of a characteristic wavelength and the associated small parameter is discussed in Section 3.1.3. With high material contrast, the latter can be the seat of local resonances. Introducing the wavenumber $k_i = \omega\sqrt{\rho_i/\mu_i}$ within the inclusions, then such resonances can occur when the wavelength within an inclusion is of order of h, i.e. $k_i h = \mathcal{O}(1)$ Auriault and Boutin (2012); Pham et al. (2017). In particular, this assumption is met for a low contrast in mass density $\rho_i/\rho_m = \mathcal{O}(1)$ and a high contrast in shear modulus $\mu_i/\mu_m = \mathcal{O}(\eta^2)$, a configuration which we consider in the present study. These geometrical and material assumptions are summarized as follows:

Assumptions 1. *The configuration satisfies* $\eta = k_m h \ll 1$ *while* $\rho_i/\rho_m = \mathcal{O}(1)$ *and* $\mu_i/\mu_m = \mathcal{O}(\eta^2)$.

2.1. *Effective jump conditions in the time domain*

New adimensionalized space-time coordinates are introduced to formulate the homogenization problem independently of the wavelength λ, i.e. one defines $\boldsymbol{x} = k_m \boldsymbol{X}$ and $\tau = k_m \sqrt{\frac{\mu_m}{\rho_m}}\, t$. One introduces the non-dimensionalized fields $v(\boldsymbol{x},\tau) = \sqrt{\frac{\rho_m}{\mu_m}} V(\boldsymbol{X},t)$ and $\boldsymbol{\sigma}(\boldsymbol{x},\tau) = \frac{1}{\mu_m}\boldsymbol{\Sigma}(\boldsymbol{X},t)$. The system (1) is then transformed into:

$$\begin{cases} \dfrac{\partial \boldsymbol{\sigma}}{\partial \tau}(\boldsymbol{x},\tau) = \dfrac{\mu}{\mu_m} \boldsymbol{\nabla}_{\boldsymbol{x}}\, v(\boldsymbol{x},\tau), \\ \dfrac{\rho}{\rho_m}\dfrac{\partial v}{\partial \tau}(\boldsymbol{x},\tau) = \mathrm{div}_{\boldsymbol{x}}\, \boldsymbol{\sigma}(\boldsymbol{x},\tau), \end{cases} \tag{2}$$

while the continuity conditions on v and $\boldsymbol{\sigma}\cdot\boldsymbol{n}$ at the matrix/inclusion interfaces are preserved.

2.1.1. *Matched asymptotic expansions*

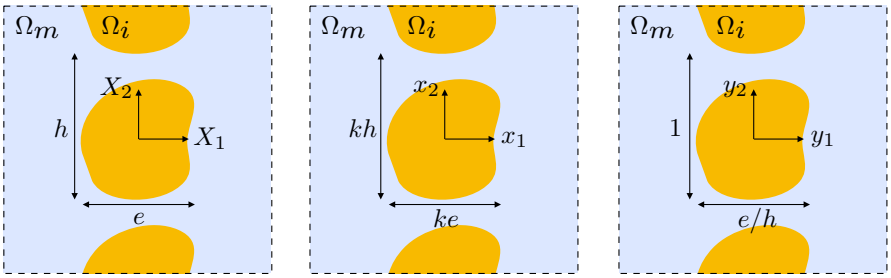

Figure 2: The different coordinate systems considered: *(left)* original coordinates, *(center)* adimensionalized coordinates, and *(right)* rescaled coordinates.

While the space coordinate $\boldsymbol{x} = (x_1, x_2)$ is appropriate to describe the *slow* variations of the wavefield, one introduces the *rescaled* coordinate $\boldsymbol{y} = \boldsymbol{x}/\eta$, see Figure 2, which will be used to describe its small-scale *fast* variations. Note that, with a slight abuse of notation, the inclusion domain is referred to as $\cup_i \Omega_i$ in all three coordinate systems. Depending on the region of space considered, the fields v and $\boldsymbol{\sigma}$ will be assumed to have specific dependencies on $\boldsymbol{x}$ and $\boldsymbol{y}$. In the far field, only the slow coordinate $\boldsymbol{x}$ is needed to describe the propagating field. Near the inclusions, dependence on the fast coordinate $\boldsymbol{y}$ is considered in order to describe field variations at the scale of the microstructure while slower variations along the interface are also accounted for through a dependence on x_2. Three regions are thus defined: an outer region (far field) for which $\boldsymbol{x} \in \mathbb{R}^2$, an inner region (near field) that excludes the inclusions, i.e. $\boldsymbol{y} \in \mathbb{R}^2 \setminus \cup_i \Omega_i$ and $x_2 \in \mathbb{R}$, and the inner region that coincides with the inclusions, i.e. $\boldsymbol{y} \in \cup_i \Omega_i$ and $x_2 \in \mathbb{R}$. In these three regions, the velocity and stress fields are expanded using the following ansatz:

Outer region ($\boldsymbol{x} \in \mathbb{R}^2$)	Inner region ($\boldsymbol{y} \in \mathbb{R}^2 \setminus \cup_i \Omega_i,\ x_2 \in \mathbb{R}$)	Inclusions region ($\boldsymbol{y} \in \cup_i \Omega_i,\ x_2 \in \mathbb{R}$)
$\begin{cases} v = \sum_{j\geq 0} \eta^j v^j(\boldsymbol{x},\tau) \\ \boldsymbol{\sigma} = \sum_{j\geq 0} \eta^j \boldsymbol{\sigma}^j(\boldsymbol{x},\tau) \end{cases}$	$\begin{cases} v = \sum_{j\geq 0} \eta^j w^j(\boldsymbol{y},x_2,\tau) \\ \boldsymbol{\sigma} = \sum_{j\geq 0} \eta^j \boldsymbol{s}^j(\boldsymbol{y},x_2,\tau) \end{cases}$	$\begin{cases} v = \sum_{j\geq 0} \eta^j w_i^j(\boldsymbol{y},x_2,\tau) \\ \boldsymbol{\sigma} = \sum_{j\geq 0} \eta^j \boldsymbol{s}_i^j(\boldsymbol{y},x_2,\tau). \end{cases}$

(3)

The terms $(w^j, \boldsymbol{s}^j)_{j\geq 0}$ of the expansion of the solution $(v, \boldsymbol{\sigma})$ in the inner region are assumed to be periodic with respect to y_2. In addition, the continuity conditions on the inclusions interfaces read $w^j = w_i^j$ and $\boldsymbol{s}^j \cdot \boldsymbol{n} = \boldsymbol{s}_i^j \cdot \boldsymbol{n}$ on $\partial\Omega_i$. We consider the bounded domain described in $\boldsymbol{y}$-coordinates as $\Omega^b = [-y_1^b, y_1^b] \times [-1/2, 1/2]$ with $y_1^b > e/h$, see Figure 3. Later on, Ω_i will denote the inclusion in this bounded elementary cell. Moreover, one introduces the domain $\Omega = \lim_{y_1^b \to \pm\infty} \Omega^b = \mathbb{R} \times [-1/2, 1/2]$ which is the *elementary cell* generating the periodic row of inclusions.

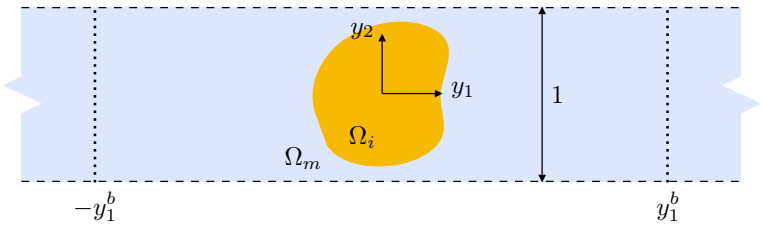

Figure 3: Bounded elementary cell $\Omega^b = [-y_1^b, y_1^b] \times [-\frac{1}{2}, \frac{1}{2}]$ with $y_1^b > \frac{e}{h}$.

As is customary in the two-scale asymptotic expansion approach, the differential operators featured in (2) are rewritten in the inner regions as:

$$\boldsymbol{\nabla}_{\boldsymbol{x}}\, v \to \frac{1}{\eta}\boldsymbol{\nabla}_{\boldsymbol{y}}\, v + \frac{\partial v}{\partial x_2}\boldsymbol{e}_2 \qquad \text{and} \qquad \operatorname{div}_{\boldsymbol{x}} \boldsymbol{\sigma} \to \frac{1}{\eta}\operatorname{div}_{\boldsymbol{y}} \boldsymbol{\sigma} + \frac{\partial \boldsymbol{\sigma}}{\partial x_2} \cdot \boldsymbol{e}_2$$

in terms of the canonical unit vectors $\boldsymbol{e}_1, \boldsymbol{e}_2$.

Inserting (3) in (2) while using the previous differential operator identities, one can identify the $\mathcal{O}(\eta^{-1})$-terms in the inner region:

$$\begin{cases} \boldsymbol{\nabla}_{\boldsymbol{y}}\, w^0 = \boldsymbol{0}, & \text{(4a)} \\ \operatorname{div}_{\boldsymbol{y}} \boldsymbol{s}^0 = 0. & \text{(4b)} \end{cases}$$

Then, in all three regions, the $\mathcal{O}(1)$-terms read

$$\begin{cases} \dfrac{\partial \boldsymbol{\sigma}^0}{\partial \tau} = \boldsymbol{\nabla}_{\boldsymbol{x}}\, v^0, & \text{(5a)} \\ \dfrac{\partial v^0}{\partial \tau} = \operatorname{div}_{\boldsymbol{x}} \boldsymbol{\sigma}^0, & \text{(5b)} \\ \dfrac{\partial \boldsymbol{s}^0}{\partial \tau} = \dfrac{\partial w^0}{\partial x_2}\boldsymbol{e}_2 + \boldsymbol{\nabla}_{\boldsymbol{y}}\, w^1, & \text{(5c)} \\ \dfrac{\partial w^0}{\partial \tau} = \dfrac{\partial \boldsymbol{s}^0}{\partial x_2} \cdot \boldsymbol{e}_2 + \operatorname{div}_{\boldsymbol{y}} \boldsymbol{s}^1, & \text{(5d)} \\ \dfrac{\partial \boldsymbol{s}_i^0}{\partial \tau} = \boldsymbol{0}, & \text{(5e)} \\ \dfrac{\rho_i}{\rho_m}\dfrac{\partial w_i^0}{\partial \tau} = \dfrac{\partial \boldsymbol{s}_i^0}{\partial x_2} \cdot \boldsymbol{e}_2 + \operatorname{div}_{\boldsymbol{y}} \boldsymbol{s}_i^1. & \text{(5f)} \end{cases}$$

Assuming that at the initial time $\boldsymbol{s}_i^0(\boldsymbol{y}, x_2, 0) = 0$, then (5e) implies

$$\boldsymbol{s}_i^0(\boldsymbol{y}, x_2, \tau) = 0 \qquad \forall \tau \geq 0. \tag{6}$$

Based on Assumptions 1, we rewrite the parameter μ_i as $\mu_i = \eta^2 \mu_0$ where μ_0 is a reference modulus that satisfies $\mu_0/\mu_m = \mathcal{O}(1)$. Doing so, then the $\mathcal{O}(\eta)$-term within the inclusions reads

$$\frac{\partial \boldsymbol{s}_i^1}{\partial \tau} = \frac{\mu_0}{\mu_m} \boldsymbol{\nabla}_{\boldsymbol{y}} w_i^0. \tag{7}$$

Finally, the outer and the inner solutions have to match in an intermediate region. Therefore, matching conditions are formulated in the limit $y_1 \to \pm\infty$ for the near-field solution and $x_1 \to 0^{\pm}$ for the far-field solution. Upon using a first-order Taylor expansion of the outer solution at $x_1 = 0$ as $v^j(x_1, x_2, \tau) = v^j(0^{\pm}, x_2, \tau) + \eta\, y_1 \partial_{x_1} v^j(0^{\pm}, x_2, \tau)$, then the $\mathcal{O}(1)$-terms are identified:

$$\begin{cases} v^0(0^{\pm}, x_2, \tau) = \lim\limits_{y_1 \to \pm\infty} w^0(\boldsymbol{y}, x_2, \tau), & \text{(8a)} \\ \boldsymbol{\sigma}^0(0^{\pm}, x_2, \tau) = \lim\limits_{y_1 \to \pm\infty} \boldsymbol{s}^0(\boldsymbol{y}, x_2, \tau), & \text{(8b)} \end{cases}$$

and the $\mathcal{O}(\eta)$-terms give:

$$\begin{cases} v^1(0^{\pm}, x_2, \tau) = \lim\limits_{y_1 \to \pm\infty} \left[w^1(\boldsymbol{y}, x_2, \tau) - y_1 \dfrac{\partial v^0}{\partial x_1}(0^{\pm}, x_2, \tau) \right], & \text{(9a)} \\ \boldsymbol{\sigma}^1(0^{\pm}, x_2, \tau) = \lim\limits_{y_1 \to \pm\infty} \left[\boldsymbol{s}^1(\boldsymbol{y}, x_2, \tau) - y_1 \dfrac{\partial \boldsymbol{\sigma}^0}{\partial x_1}(0^{\pm}, x_2, \tau) \right]. & \text{(9b)} \end{cases}$$

2.1.2. Jump conditions at the order $\mathcal{O}(1)$

The homogenization of such a periodic row of highly-contrasted inclusions using matched asymptotic expansions has been investigated in Pham et al. (2017) in the frequency domain. We follow the same method here and underline only the differences due to the time-domain approach for the derivation of the jump conditions at the two first orders. Introducing for any function $f(x_1)$ the notation $[\![f]\!] = f(0^+) - f(0^-)$ then the jump condition for v^0 reads:

$$[\![v^0(\cdot, x_2, \tau)]\!] = 0, \tag{10}$$

as well as the jump condition for σ_1^0:

$$[\![\sigma_1^0(\cdot, x_2, \tau)]\!] = 0. \tag{11}$$

Remark 1. *We assume that v^0 and σ_1^0 are sufficiently smooth so that $\frac{\partial}{\partial \zeta} [\![v^0(\cdot, x_2, \tau)]\!] = [\![\frac{\partial}{\partial \zeta} v^0(\cdot, x_2, \tau)]\!]$ and $\frac{\partial}{\partial \zeta} [\![\sigma_1^0(\cdot, x_2, \tau)]\!] = [\![\frac{\partial}{\partial \zeta} \sigma_1^0(\cdot, x_2, \tau)]\!]$ for $\zeta = x_2$ or $\zeta = \tau$. Hence equations (10) and (11) imply:*

$$\left[\!\!\left[\frac{\partial}{\partial \zeta} v^0(\cdot, x_2, \tau) \right]\!\!\right] = 0, \tag{12}$$

and

$$\left[\!\!\left[\frac{\partial}{\partial \zeta} \sigma_1^0(\cdot, x_2, \tau) \right]\!\!\right] = 0, \tag{13}$$

for $\zeta = x_2$ or τ.

2.1.3. Jump conditions at the order $\mathcal{O}(\eta)$

Jump condition for v^1. The same approach as in the frequency domain Pham et al. (2017) leads to the following jump condition:

$$\left[\!\left[v^1(\cdot, x_2, \tau)\right]\!\right] = B_1 \frac{\partial v^0}{\partial x_1}(0, x_2, \tau) + B_2 \frac{\partial v^0}{\partial x_2}(0, x_2, \tau). \tag{14}$$

The constants B_j are introduced for $j = 1, 2$:

$$B_j = \lim_{y_1 \to +\infty} \left[\Phi^{(j)}(y_1, y_2) - \Phi^{(j)}(-y_1, y_2)\right], \tag{15}$$

with for $j = 1, 2$ the fields $\Phi^{(j)}$ being y_2-periodic and solutions of:

$$\begin{cases} \Delta_{\boldsymbol{y}} \Phi^{(j)}(\boldsymbol{y}) = 0 & \text{in } \Omega \backslash \Omega_i, \\ [\boldsymbol{\nabla}_{\boldsymbol{y}} \Phi^{(j)}(\boldsymbol{y}) + \boldsymbol{e}_j] \cdot \boldsymbol{n} = 0 & \text{on } \partial\Omega_i, \\ \lim\limits_{y_1 \to \pm\infty} \boldsymbol{\nabla}_{\boldsymbol{y}} \Phi^{(j)}(y_1, y_2) = \boldsymbol{0}. \end{cases} \tag{16}$$

Jump condition for σ_1^1. Using both (12) and (13) with $\zeta = x_2$ and $\zeta = \tau$ together with (5a) and (5b) implies that $\frac{\partial}{\partial x_1}\sigma_1^0(\cdot, x_2, \tau)$ is continuous at $x_1 = 0$. The equation (9b) integrated along $y_2 \in [-1/2, 1/2]$ provides the jump condition for σ_1^1:

$$\left[\!\left[\sigma_1^1(\cdot, x_2, \tau)\right]\!\right] = \lim_{y_1^b \to +\infty} \int_{-\frac{1}{2}}^{\frac{1}{2}} \left[s_1^1(y_1^b, y_2, x_2, \tau) - s_1^1(-y_1^b, y_2, x_2, \tau)\right] \mathrm{d}y_2 - 2y_1^b \frac{\partial \sigma_1^0}{\partial x_1}(0, x_2, \tau).$$

We start with (5d) integrated on $\Omega^b \backslash \Omega_i$:

$$\underbrace{\int_{\Omega^b \backslash \Omega_i} \frac{\partial w^0}{\partial \tau} \, \mathrm{d}\boldsymbol{y}}_{I_1} \underbrace{- \int_{\Omega^b \backslash \Omega_i} \frac{\partial \boldsymbol{s}^0}{\partial x_2} \cdot \boldsymbol{e}_2 \, \mathrm{d}\boldsymbol{y}}_{I_2} \underbrace{- \int_{\Omega^b \backslash \Omega_i} \mathrm{div}_{\boldsymbol{y}} \, \boldsymbol{s}^1 \, \mathrm{d}\boldsymbol{y}}_{I_3} = 0.$$

We introduce the parameter φ satisfying $0 < \varphi < 1$ and such that $S_i = \frac{e\varphi}{h}$ is the surface of the inclusion. The first integral I_1 can be computed:

$$I_1 = \frac{\partial v^0}{\partial \tau}(0, x_2, \tau) \left[2y_1^b - \frac{e\varphi}{h}\right]. \tag{17}$$

The derivative $\frac{\partial}{\partial \tau} s_2^0(\boldsymbol{y}, x_2, \tau)$ can be expressed thanks to the cell functions defined in (16):

$$\frac{\partial s_2^0}{\partial \tau}(\boldsymbol{y}, x_2, \tau) = \frac{\partial \sigma_1^0}{\partial \tau}(0, x_2, \tau) \frac{\partial \Phi^{(1)}}{\partial y_2}(\boldsymbol{y}) + \frac{\partial \sigma_2^0}{\partial \tau}(0, x_2, \tau) \left[\frac{\partial \Phi^{(2)}}{\partial y_2}(\boldsymbol{y}) + 1\right], \tag{18}$$

so that the second integral I_2 writes:

$$I_2 = -\frac{\partial \sigma_1^0}{\partial x_2}(0, x_2, \tau) \int_{\Omega^b \backslash \Omega_i} \frac{\partial \Phi^{(1)}}{\partial y_2}(\boldsymbol{y}) - \frac{\partial \sigma_2^0}{\partial x_2}(0, x_2, \tau) \left[\int_{\Omega^b \backslash \Omega_i} \frac{\partial \Phi^{(2)}}{\partial y_2}(\boldsymbol{y}) + 2y_1^b - \frac{e\varphi}{h}\right]. \tag{19}$$

Owing to the periodicity of $\boldsymbol{s}^1$ with respect to y_2 and introducing the curvilinear abscissa ℓ on $\partial\Omega_i$, with $\boldsymbol{n}$ being the associated *inward* unit normal, then I_3 can be expressed as

$$I_3 = -\int_{-\frac{1}{2}}^{\frac{1}{2}} [s_1^1(y_1^b, y_2, x_2, \tau) - s_1^1(-y_1^b, y_2, x_2, \tau)]\,\mathrm{d}y_2 - \int_{\partial\Omega_i} \boldsymbol{s}^1 \cdot \boldsymbol{n}\,\mathrm{d}\ell.$$

Due to the continuity condition $\boldsymbol{s}^1 \cdot \boldsymbol{n} = \boldsymbol{s}_i^1 \cdot \boldsymbol{n}$ on $\partial\Omega_i$, the second term in I_3 can be recast as

$$-\int_{\partial\Omega_i} \boldsymbol{s}^1 \cdot \boldsymbol{n}\,\mathrm{d}\ell = \int_{\Omega_i} \mathrm{div}_{\boldsymbol{y}}\, \boldsymbol{s}_i^1\,\mathrm{d}\boldsymbol{y}.$$

We now use (5f) together with (6) and (7). For the boundary condition, the continuity condition $w^j = w_i^j$ on $\partial\Omega_i$ and (4a) with (8a) is used. Then, the field $\boldsymbol{s}_i^1$ satisfies

$$\begin{cases} \dfrac{\partial \boldsymbol{s}_i^1}{\partial\tau}(\boldsymbol{y}, x_2, \tau) = \dfrac{\mu_0}{\mu_m} \boldsymbol{\nabla}_{\boldsymbol{y}}\, w_i^0(\boldsymbol{y}, x_2, \tau) & (\boldsymbol{y} \in \Omega_i), \\ \dfrac{\rho_i}{\rho_m} \dfrac{\partial w_i^0}{\partial\tau}(\boldsymbol{y}, x_2, \tau) = \mathrm{div}_{\boldsymbol{y}}\, \boldsymbol{s}_i^1(\boldsymbol{y}, x_2, \tau) & (\boldsymbol{y} \in \Omega_i), \\ w_i^0(\boldsymbol{y}, x_2, \tau) = v^0(0, x_2, \tau) & (\boldsymbol{y} \in \partial\Omega_i). \end{cases}$$

Therefore, one concludes that the field w_i^0 is solution of

$$\begin{cases} \dfrac{\rho_i}{\rho_m} \dfrac{\partial^2 w_i^0}{\partial\tau^2}(\boldsymbol{y}, x_2, \tau) - \dfrac{\mu_0}{\mu_m} \Delta_{\boldsymbol{y}} w_i^0(\boldsymbol{y}, x_2, \tau) = 0 & (\boldsymbol{y} \in \Omega_i), \\ w_i^0(\boldsymbol{y}, x_2, \tau) = v^0(0, x_2, \tau) & (\boldsymbol{y} \in \partial\Omega_i), \end{cases} \tag{20}$$

and one can rewrite

$$I_3 = -\int_{-\frac{1}{2}}^{\frac{1}{2}} [s_1^1(y_1^b, y_2, x_2, \tau) - s_1^1(-y_1^b, y_2, x_2, \tau)]\,\mathrm{d}y_2 + \frac{\rho_i}{\rho_m} \int_{\Omega_i} \frac{\partial w_i^0}{\partial\tau}\,\mathrm{d}\boldsymbol{y}. \tag{21}$$

Collecting the three integrals (17), (19) and (21) and using (5b) one gets

$$\begin{aligned} &\int_{-\frac{1}{2}}^{\frac{1}{2}} [s_1^1(y_1^b, y_2, x_2, \tau) - s_1^1(-y_1^b, y_2, x_2, \tau)]\,\mathrm{d}y_2 - 2y_1^b \frac{\partial\sigma_1^0}{\partial x_1}(0, x_2, \tau) = -\frac{e\varphi}{h} \frac{\partial\sigma_1^0}{\partial x_1}(0, x_2, \tau) \\ &- \frac{\partial\sigma_1^0}{\partial x_2}(0, x_2, \tau) \int_{\Omega^b\setminus\Omega_i} \frac{\partial\Phi^{(1)}}{\partial y_2}(\boldsymbol{y})\,\mathrm{d}\boldsymbol{y} - \frac{\partial\sigma_2^0}{\partial x_2}(0, x_2, \tau) \int_{\Omega^b\setminus\Omega_i} \frac{\partial\Phi^{(2)}}{\partial y_2}(\boldsymbol{y})\,\mathrm{d}\boldsymbol{y} + \frac{\rho_i}{\rho_m} \int_{\Omega_i} \frac{\partial w_i^0}{\partial\tau}\,\mathrm{d}\boldsymbol{y}. \end{aligned} \tag{22}$$

Introducing the following two parameters

$$C_j = -\int_{\Omega\setminus\Omega_i} \frac{\partial\Phi^{(j)}}{\partial y_2}(\boldsymbol{y})\,\mathrm{d}\boldsymbol{y} \qquad \text{for } j = 1, 2 \tag{23}$$

and taking the limit $y_1^b \to +\infty$ in (22) finally entails the following jump condition

$$[\![\sigma_1^1(\cdot, x_2, \tau)]\!] = -\frac{e\varphi}{h} \frac{\partial\sigma_1^0}{\partial x_1}(0, x_2, \tau) + C_1 \frac{\partial\sigma_1^0}{\partial x_2}(0, x_2, \tau) + C_2 \frac{\partial\sigma_2^0}{\partial x_2}(0, x_2, \tau) + \frac{\rho_i}{\rho_m} \int_{\Omega_i} \frac{\partial w_i^0}{\partial\tau}\,\mathrm{d}\boldsymbol{y}. \tag{24}$$

2.1.4. Final effective jump conditions

The jump conditions derived in the previous sections are associated with an interface of zero thickness as one considers jumps in the limit $x_1 \to 0^{\pm}$. Yet, it has been shown in Marigo and Maurel (2016) and Marigo et al. (2017) that a non-zero thickness a allows to define an interface energy, which would in turn ensure the stability of the effective model. Using such an energy-based argument, we will justify in the next section that an enlarged interface is also required in the resonant case considered here. Meanwhile, the present section establishes the final effective jump conditions expressed relatively to an enlarged interface of thickness $a > 0$ in the original system of space coordinates with $a/h = \mathcal{O}(1)$. The effective jump conditions thus obtained are equivalent up to order $\mathcal{O}(\eta^2)$ to the ones formulated in Section 2.1.3.

For any function $f(x_1)$, we define the jump and the mean value around the (centered) enlarged interface of thickness a:

$$\llbracket f \rrbracket_{k_m a} = f(k_m a/2) - f(-k_m a/2) \qquad \text{and} \qquad \langle f \rangle_{k_m a} = \frac{1}{2}\big(f(k_m a/2) + f(-k_m a/2)\big).$$

Setting $f = v(\cdot, x_2, \tau)$ or $f = \sigma_1(\cdot, x_2, \tau)$, we seek asymptotics of the form:

$$\llbracket f \rrbracket_{k_m a} = \llbracket f^0 \rrbracket_{k_m a} + \eta \, \llbracket f^1 \rrbracket_{k_m a} + \mathcal{O}(\eta^2). \tag{25}$$

To do so, we consider the following Taylor expansions between $0^{\pm}$ and $\pm k_m a/2$ for the function f defined above

$$\begin{cases} \llbracket f^0 \rrbracket = \llbracket f^0 \rrbracket_{k_m a} - \eta \dfrac{a}{h} \left\langle \dfrac{\partial f^0}{\partial x_1} \right\rangle_{k_m a} + \mathcal{O}(\eta^2), \\ \llbracket f^1 \rrbracket = \llbracket f^1 \rrbracket_{k_m a} + \mathcal{O}(\eta). \end{cases} \tag{26}$$

Likewise for $g = \partial v^0/\partial x_j(\cdot, x_2, \tau)$ or $g = \partial \sigma_k^0/\partial x_j(\cdot, x_2, \tau)$ with $j, k = 1, 2$ one considers

$$g(0) = \langle g \rangle_{k_m a} + \mathcal{O}(\eta). \tag{27}$$

Due to (27), the solution to (20) is expanded as $w_i^0 = w_i + \mathcal{O}(\eta)$ where the field w_i is solution to the inner problem

$$\begin{cases} \dfrac{\rho_i}{\rho_m} \dfrac{\partial^2 w_i}{\partial \tau^2}(\boldsymbol{y}, x_2, \tau) - \dfrac{\mu_0}{\mu_m} \Delta_{\boldsymbol{y}} w_i(\boldsymbol{y}, x_2, \tau) = 0 & (\boldsymbol{y} \in \Omega_i), \\ w_i(\boldsymbol{y}, x_2, \tau) = \langle v(\cdot, x_2, \tau) \rangle_{k_m a} & (\boldsymbol{y} \in \partial\Omega_i). \end{cases} \tag{28}$$

Introducing the following coefficients

$$S = \frac{a}{h} - \frac{e\varphi}{h} \qquad \text{and} \qquad B = \frac{a}{h} + B_1, \tag{29}$$

then combining the equations (25–27), (10), (14), (11), (24) and (28), we get

$$\begin{cases} \llbracket v \rrbracket_{k_m a} = \eta \left\{ B \left\langle \dfrac{\partial v}{\partial x_1} \right\rangle_{k_m a} + B_2 \left\langle \dfrac{\partial v}{\partial x_2} \right\rangle_{k_m a} \right\} + \mathcal{O}(\eta^2), \\ \llbracket \sigma_1 \rrbracket_{k_m a} = \eta \left\{ S \left\langle \dfrac{\partial \sigma_1}{\partial x_1} \right\rangle_{k_m a} + C_1 \left\langle \dfrac{\partial \sigma_1}{\partial x_2} \right\rangle_{k_m a} + C_2 \left\langle \dfrac{\partial \sigma_2}{\partial x_2} \right\rangle_{k_m a} + \dfrac{\rho_i}{\rho_m} \displaystyle\int_{\Omega_i} \frac{\partial w_i}{\partial \tau} \, \mathrm{d}\boldsymbol{y} \right\} + \mathcal{O}(\eta^2). \end{cases}$$

We now consider the associated approximation of the fields, as $(v^h, \boldsymbol{\sigma}^h) = (v^0 + \eta v^1, \boldsymbol{\sigma}^0 + \eta \boldsymbol{\sigma}^1)$, which are solution to (2) in the matrix domain while satisfying the jump conditions above but truncated at

the second order. These fields are then transposed in the original coordinate system $(\boldsymbol{X}, t)$, see Figure 2, as $(V^h, \boldsymbol{\Sigma}^h)$, to get finally the following effective model at order $\mathcal{O}(\eta)$:

$$\begin{cases} \dfrac{\partial \boldsymbol{\Sigma}^h}{\partial t} = \mu_m \boldsymbol{\nabla} V^h & (|X_1| \geq a/2,\ X_2 \in \mathbb{R}), \\ \rho_m \dfrac{\partial V^h}{\partial t} = \operatorname{div} \boldsymbol{\Sigma^h} & (|X_1| \geq a/2,\ X_2 \in \mathbb{R}), \\ \left[\!\left[V^h \right]\!\right]_a = h \left\{ B \left\langle \dfrac{\partial V^h}{\partial X_1} \right\rangle_a + B_2 \left\langle \dfrac{\partial V^h}{\partial X_2} \right\rangle_a \right\} & (X_2 \in \mathbb{R}), \\ \left[\!\left[\Sigma_1^h \right]\!\right]_a = h \left\{ S \left\langle \dfrac{\partial \Sigma_1^h}{\partial X_1} \right\rangle_a + C_1 \left\langle \dfrac{\partial \Sigma_1^h}{\partial X_2} \right\rangle_a + C_2 \left\langle \dfrac{\partial \Sigma_2^h}{\partial X_2} \right\rangle_a + \rho_i \displaystyle\int_{\Omega_i} \dfrac{\partial W_i}{\partial t} \, \mathrm{d}\boldsymbol{y} \right\} & (X_2 \in \mathbb{R}). \end{cases} \tag{30}$$

In (30), $W_i(\boldsymbol{y}, X_2, t) = \sqrt{\frac{\mu_m}{\rho_m}}\, w_i(\boldsymbol{y}, x_2, \tau)$ so that W_i is solution of

$$\begin{cases} \dfrac{\partial \boldsymbol{\Sigma}_i}{\partial t}(\boldsymbol{y}, X_2, t) = \dfrac{\mu_i}{h} \boldsymbol{\nabla}_{\boldsymbol{y}} W_i(\boldsymbol{y}, X_2, t) & (\boldsymbol{y} \in \Omega_i), \\ \rho_i \dfrac{\partial W_i}{\partial t}(\boldsymbol{y}, X_2, t) = \dfrac{1}{h} \operatorname{div}_{\boldsymbol{y}} \boldsymbol{\Sigma}_i(\boldsymbol{y}, X_2, t) & (\boldsymbol{y} \in \Omega_i), \\ W_i(\boldsymbol{y}, X_2, t) = \left\langle V^h(\cdot, X_2, t) \right\rangle_a & (\boldsymbol{y} \in \partial\Omega_i). \end{cases} \tag{31}$$

One notices that the field W_i is a function of X_2 through the prescribed boundary condition $\langle V^h(\cdot, X_2, t)\rangle_a$. The five effective parameters B, B_2, S, C_1 and C_2 are given by (29), (15), and (23).

Remark 2. *The equivalence between this model and the one obtained in the frequency-domain in Pham et al. (2017) is assessed in Appendix Appendix A.*

2.2. Energy analysis

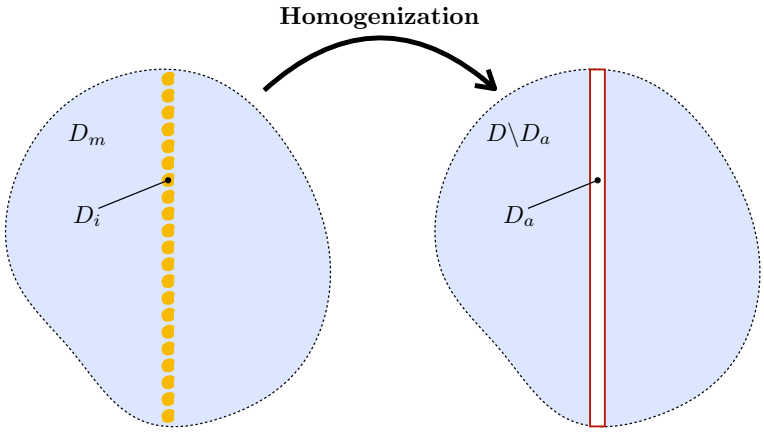

Figure 4: *(left)* Domain $D = \cup_i D_i \cup D_m$ considered for the energy analysis in the original microstructured configuration, *(right)* domain $D\backslash D_a$ for the analysis of the effective problem.

One advantage of the time-domain formulation is the possibility to perform an energy analysis, which is under study in this section. In the original microstructured configuration, a bounded domain

$D = \cup_i D_i \cup D_m$ is considered in order to define the elastic energy. Accordingly, in the homogenized problem, the elastic energy has to be defined in the bounded domain $D\backslash D_a$ that excludes the enlarged interface of width a, see Figure 4. In this configuration, a term $\mathcal{E}_a$ will be associated to the jump conditions at the effective interface. We expect it to account for the *bulk* energy of the microstructured region of thickness e in the original problem, so that $\mathcal{E}_a \geq 0$ is expected.

Multiplying the first equation of (30) by $\boldsymbol{\Sigma}^h$, the second by V^h, then after summation and integration over $D\backslash D_a$ one obtains:

$$\frac{\mathrm{d}}{\mathrm{d}t}\underbrace{\frac{1}{2}\int_{D\backslash D_a}\left\{\frac{1}{\mu_m}(\boldsymbol{\Sigma}^h)^2+\rho_m(V^h)^2\right\}\mathrm{d}\boldsymbol{X}}_{\mathcal{E}}+\underbrace{\int_I \left[\!\left[V^h\boldsymbol{\Sigma}^h\cdot\boldsymbol{e}_1\right]\!\right]_a \mathrm{d}X_2}_{\frac{\mathrm{d}}{\mathrm{d}t}\mathcal{E}_a}+\int_{\partial D} V^h\boldsymbol{\Sigma}^h\cdot\boldsymbol{n}\,\mathrm{d}\ell=0, \quad (32)$$

where the interval I is defined as $I=\{X_2 : \boldsymbol{X}\in D_a\}$ and $\boldsymbol{n}$ is the *inward* unit normal on ∂D. $\mathcal{E}$ and $\mathcal{E}_a$ are respectively some *bulk* and interface energy terms.

Focusing on the term $\mathcal{E}_a$, then using the relation $[\![fg]\!]_a = [\![f]\!]_a \langle g\rangle_a + [\![g]\!]_a \langle f\rangle_a$ together with the jump conditions of (30) one obtains

$$\begin{aligned}\frac{\mathrm{d}}{\mathrm{d}t}\mathcal{E}_a &= \int_I h\left\{B\left\langle\frac{\partial V^h}{\partial X_1}\right\rangle_a + B_2\left\langle\frac{\partial V^h}{\partial X_2}\right\rangle_a\right\}\left\langle\Sigma_1^h\right\rangle_a \mathrm{d}X_2\\ &+\int_I h\left\{S\left\langle\frac{\partial \Sigma_1^h}{\partial X_1}\right\rangle_a + C_1\left\langle\frac{\partial \Sigma_1^h}{\partial X_2}\right\rangle_a + C_2\left\langle\frac{\partial \Sigma_2^h}{\partial X_2}\right\rangle_a\right\}\left\langle V^h\right\rangle_a \mathrm{d}X_2 + J,\end{aligned}$$

where one has defined

$$J = h\rho_i\int_I\left\{\int_{\Omega_i}\frac{\partial W_i}{\partial t}(\boldsymbol{y},X_2,t)\,\mathrm{d}\boldsymbol{y}\right\}\left\langle V^h\right\rangle_a \mathrm{d}X_2. \quad (33)$$

The first two relations of (30) and integration by parts lead to

$$\begin{aligned}\frac{\mathrm{d}}{\mathrm{d}t}\mathcal{E}_a &= \beta + \frac{h}{2}\frac{\mathrm{d}}{\mathrm{d}t}\int_I\left\{S\rho_m\left\langle V^h\right\rangle_a^2 + \frac{B}{\mu_m}\left\langle\Sigma_1^h\right\rangle_a^2 + \frac{S-C_2}{\mu_m}\left\langle\Sigma_2^h\right\rangle_a^2\right\}\mathrm{d}X_2\\ &+ h(B_2-C_1)\int_I\left\langle\frac{\partial V^h}{\partial X_2}\right\rangle_a\left\langle\Sigma_1^h\right\rangle_a + J,\end{aligned}$$

where β is a boundary term on ∂I.

Adapting the proof of Appendix A in Marigo et al. (2017) with an integration in the domain $\Omega\backslash\Omega_i$, it is straightforward to show from (16) that one has

$$B_2 = C_1 = \int_{\Omega\backslash\Omega_i}\boldsymbol{\nabla}_{\boldsymbol{y}}\Phi^{(1)}\cdot\boldsymbol{\nabla}_{\boldsymbol{y}}\Phi^{(2)}\,\mathrm{d}\boldsymbol{y}.$$

The term involving $\mathcal{E}_a$ reduces to

$$\frac{\mathrm{d}}{\mathrm{d}t}\mathcal{E}_a = \beta + \frac{h}{2}\frac{\mathrm{d}}{\mathrm{d}t}\int_I\left\{S\rho_m\left\langle V^h\right\rangle_a^2 + \frac{B}{\mu_m}\left\langle\Sigma_1^h\right\rangle_a^2 + \frac{S-C_2}{\mu_m}\left\langle\Sigma_2^h\right\rangle_a^2\right\}\mathrm{d}X_2 + J. \quad (34)$$

Next, we want to express J in (33) as a quadratic form. To do so, we use the field equations and the boundary conditions in (31) to rewrite J as follows:

$$\begin{aligned}J &= -\int_I\int_{\partial\Omega_i}\boldsymbol{\Sigma}_i(\boldsymbol{y},X_2,t)\cdot\boldsymbol{n}\left\langle V^h(\cdot,X_2,t)\right\rangle_a \mathrm{d}\boldsymbol{y}\,\mathrm{d}X_2,\\ &= \int_I\int_{\Omega_i}\left\{W_i\ \mathrm{div}_{\boldsymbol{y}}\,\boldsymbol{\Sigma}_i + \boldsymbol{\Sigma}_i\cdot\boldsymbol{\nabla}_{\boldsymbol{y}}W_i\right\}\mathrm{d}\boldsymbol{y}\,\mathrm{d}X_2,\end{aligned}$$

from which one gets

$$J = \frac{1}{2}\frac{\mathrm{d}}{\mathrm{d}t}\int_I\int_{\Omega_i}\left\{h\rho_i {W_i}^2 + \frac{h}{\mu_i}\left|\boldsymbol{\Sigma}_i\right|^2\right\}\mathrm{d}\boldsymbol{y}\,\mathrm{d}X_2.$$

Finally, the interface term (34) is recast as

$$\begin{aligned}\frac{\mathrm{d}}{\mathrm{d}t}\mathcal{E}_a = \beta + \frac{h}{2}\frac{\mathrm{d}}{\mathrm{d}t}\int_I\left\{S\rho_m\left\langle V^h\right\rangle_a^2 + \frac{B}{\mu_m}\left\langle\Sigma_1^h\right\rangle_a^2 + \frac{S-C_2}{\mu_m}\left\langle\Sigma_2^h\right\rangle_a^2\right\}\mathrm{d}X_2 \\ + \frac{h}{2}\frac{\mathrm{d}}{\mathrm{d}t}\int_I\int_{\Omega_i}\left\{\rho_i {W_i}^2 + \frac{1}{\mu_i}\left|\boldsymbol{\Sigma}_i\right|^2\right\}\mathrm{d}\boldsymbol{y}\,\mathrm{d}X_2.\end{aligned} \tag{35}$$

To conclude, assuming that the wavefield solution to the time-domain homogenized problem has compact support, then the bounded domain D can be chosen sufficiently large so that the remaining boundary terms on ∂D in (32) and β on ∂I vanish. The identity (32) finally reads as the following conservation equation:

$$\frac{\mathrm{d}}{\mathrm{d}t}(\mathcal{E} + \mathcal{E}_a) = 0. \tag{36}$$

Lastly, the term $\mathcal{E}_a$ has to be positive to represent an energy. In this case, (36) is a conservation equation for the total energy $(\mathcal{E} + \mathcal{E}_a)$, a sufficient condition for the continuous problem considered to be stable. Since $\mathcal{E}_a$ is a quadratic form, a sufficient condition for $\mathcal{E}_a \geq 0$ is $B \geq 0$, $S \geq 0$ and $(S - C_2) \geq 0$. These three terms can be bounded below as follows:

- $S \geq 0$ if and only if $a/e \geq \varphi$.
- $B \geq 0$. This condition has been proved in the 3D case in Maurel et al. (2019b) when $a = e$. For completeness, it is proved for all a in the 2D case in Appendix Appendix B.
- $(S - C_2) \geq 0$ if $a \geq e$. This condition has been proved in the 3D case in Maurel et al. (2019b) when $a = e$. For completeness, it is proved for all a in the 2D case in Appendix Appendix C.

To sum up, provided that $a \geq e$ then $\mathcal{E}_a$ can be defined as an energy for all $0 < \varphi < 1$, which is associated with the effective interface of finite thickness a. In turn, Equation (36) ensures that the homogenized problem (30) is stable.

3. Numerical experiments

3.1. Configuration and numerical methods

3.1.1. Microstructured configuration

We consider the propagation of waves across a straight and h-periodic row of elliptic inclusions aligned with the X_2-axis and placed at $X_1 = 0\,\mathrm{m}$. One sets $h = 2\,\mathrm{m}$ and the ellipses are defined with semi-major axis $R_1 = 0.8\,\mathrm{m}$, semi-minor axis $R_2 = 0.5\,\mathrm{m}$ and tilt angle $\theta = 40°$ with respect to the X_1-axis, which results in a row thickness $e = 1.3838\,\mathrm{m}$. The inclusions are highly contrasted, with shear modulus $\mu_i = 10^{-2}\mu_m = 10^8\ \mathrm{kg}\cdot\mathrm{m}^{-1}\cdot\mathrm{s}^{-2}$ while their mass density is such that $\rho_i = \rho_m = 4.44\cdot 10^3\,\mathrm{kg}\cdot\mathrm{m}^{-3}$. The corresponding wave velocities are $c_m = 1500\,\mathrm{m}\cdot\mathrm{s}^{-1}$ and $c_i = 150\,\mathrm{m}\cdot\mathrm{s}^{-1}$.

A numerical approximation of the solution $\boldsymbol{U} = (V, \boldsymbol{\Sigma})^\top$ in this microstructured configuration is obtained using the numerical method presented in Lombard et al. (2008). The system (1) is discretized on a Cartesian grid and solved using the ADER-4 scheme Schwartzkopff et al. (2004); Lorcher and Munz (2006). As expected, the mesh size has to be much smaller than h for the inclusions geometry to be suitably approximated, which in turn implies high numerical costs in terms of computation time and memory requirements. Here, the interfaces $\partial\Omega_i$ are discretized using the Explicit Simplified Interface Method (ESIM).

3.1.2. Homogenized model

In the equivalent homogenized model (30), and owing to the analysis of Section 2.2, the interface thickness is chosen as $a = e$. The effective parameter S in (29) is calculated from the physical parameter values while the parameters B_1, B_2, C_1 and C_2 are computed numerically. Introducing the functional spaces

$$L^p_{\text{loc}}(\Omega\backslash\Omega_i) = \Big\{ f \in L^p(K\backslash\Omega_i) \text{ with } K =]-\infty,\infty[\times[a,b] \text{ for all } a \leq b \text{ such that } K \subset \Omega \Big\},$$

and

$$\mathcal{H}^{\text{per}}_{0,j}(\Omega\backslash\Omega_i) = \Big\{ \frac{\partial f}{\partial y_j} \in L^1_{\text{loc}}(\Omega\backslash\Omega_i),\ \frac{\partial f}{\partial y_k} \in L^2_{\text{loc}}(\Omega\backslash\Omega_i) \text{ for } k \neq j, \\ \text{and } \tilde{\Phi}(y_1, y_2+1) = \tilde{\Phi}(y_1, y_2) \text{ for all } \boldsymbol{y} \in \Omega\backslash\Omega_i \text{ with } \int_{\Omega\backslash\Omega_i} \tilde{\Phi}(\boldsymbol{y})\, \mathrm{d}\boldsymbol{y} = 0 \Big\},$$

then the variational formulation associated with (16) reads for all $\tilde{\Phi} \in \mathcal{H}^{\text{per}}_{0,j}(\Omega\backslash\Omega_i)$:

$$\int_{\Omega\backslash\Omega_i} \big[\boldsymbol{\nabla}_{\boldsymbol{y}}\Phi^{(j)}(\boldsymbol{y}) + \boldsymbol{e}_j\big] \cdot \boldsymbol{\nabla}_{\boldsymbol{y}}\tilde{\Phi}(\boldsymbol{y})\, \mathrm{d}\boldsymbol{y} - \lim_{y_1 \to +\infty} \int_{-1/2}^{1/2} \big[\tilde{\Phi}(y_1, y_2) - \tilde{\Phi}(-y_1, y_2)\big] \boldsymbol{e}_1 \cdot \boldsymbol{e}_j\, \mathrm{d}y_2 = 0. \quad (37)$$

The solutions $\Phi^{(j)}$ are then approximated in a bounded domain $\Omega^b\backslash\Omega_i$, where $\Omega^b = [-y^b, y^b] \times [-\frac{1}{2}, \frac{1}{2}]$ and $y^b > 0$ is chosen to be sufficiently large. These approximations are computed using the finite elements method on a single cell. Once these two cell problems are solved numerically, then the four coefficients B_1, B_2, C_1 and C_2 are approximated based on (15) and (23). For the configuration considered, the obtained values are reported in Table 1. Finally, the solution $\boldsymbol{U}^h = (V^h, \boldsymbol{\Sigma}^h)^\top$ of

Table 1: Numerical values of the effective interface parameters featured in (30).

B_1	B	B_2	S	C_1	C_2
0.911	1.603	-0.142	0.378	-0.142	0.2

the time-domain effective problem (30) is discretized with a mesh size ΔX and a time step Δt and we denote by $(\mathbf{U}^h)^n_{i,j}$ the approximation of $\boldsymbol{U}^h$ at point $(i\Delta X, j\Delta X)$ and time $t_n = n\Delta t$. A specific numerical method has been developed in Touboul et al. (2020) to handle the resonant jump conditions considered, which are non-local in time. The latter relies on the introduction of a set of *auxiliary variables*, locally along the interface, to derive some equivalent jump conditions that are local in time. The resulting system is in turn discretized on a Cartesian grid and solved using the ADER-4 scheme while the geometry of the interface is handled using an extension of the ESIM to the resonant case. We refer the reader to this reference for a detailed account on it.

In the proposed numerical method, the auxiliary variables, which are introduced to derive a local-in-time system, rely on the expression of $D(k_m)$ in (A.8). The expression of this coefficient is detailed in Appendix Appendix A. The values (α_r, k_r) are obtained by solving numerically the eigenvalue problem (A.6). The first four modes P_r of the eigenvalue problem (A.6) are shown in Figure 5 for the elliptic inclusions case considered. Referring to the discussion in Appendix Appendix A, then the modes P_1 and P_4 in Figure 5a and 5d have non-null mean values and are linked to resonances at k_1 and k_4 in $D(k_m)$. The modes P_2 and P_3 represented in Figures 5b and 5c have null mean values and the associated resonances k_2 and k_3 are not taken into account in the effective model. Numerically,

the infinite sum in $D(k_m)$ is truncated to the first eight resonances associated with modes that have non-null mean values. Computations have been performed to check that the resonances not taken into account have a negligible influence on the effective solution. The numerical values of the parameters α_0 and (α_r, k_r) for $\alpha_r \neq 0$, which are used numerically, are reported in Table 2.

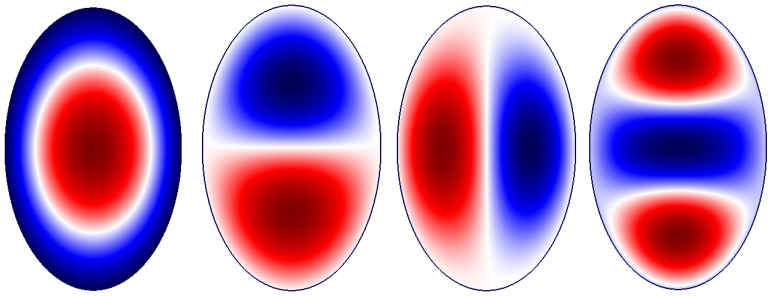

(a) P_1 (b) P_2 (c) P_3 (d) P_4

Figure 5: Four first modes P_r of the eigenvalue problem (A.6) for the elliptic inclusions considered.

Table 2: Resonances parameters in (A.8).

r	0	1	4	8	9	13	16	21	23
α_r	0.314	0.462	0.144	0.148	0.069	0.078	0.037	0.053	0.081
k_r (rad $\cdot$ m^{-1})		0.4	0.734	1.015	1.091	1.308	1.452	1.625	1.642

3.1.3. Initial condition and forcing

To design the initial conditions or the forcing term, the following source function is introduced

$$F(\xi) = \begin{cases} \displaystyle\sum_{k=0}^{3} \beta_k \sin(2^k k_m \xi) & \text{if } -\frac{c_m}{f_0} \leq \xi \leq 0 \\ 0 & \text{otherwise,} \end{cases} \tag{38}$$

with f_0 the central frequency, $\beta_0 = 1$, $\beta_1 = -21/32$, $\beta_2 = 63/768$, and $\beta_3 = -1/512$, which entails that F is of class C^6. Figure 6 displays the Fourier transform $\hat{F}$ of F as a function of $f = kc_m/(2\pi)$ for $f_0 \in \{25, 50, 100\}$ Hz. The small parameter corresponding to these central frequencies reads $\eta(f_0) \in \{0.21, 0.42, 0.84\}$, respectively. While in Fig. 6 the dashed line indicates the central frequency f_0, it should be noted that the frequency content of F extends to frequencies much higher than f_0 thus resulting in higher values of the parameter η for the associated wavelengths. In this figure, the blue crosses denote the resonant frequencies $f_r = k_r c_m/(2\pi)$ in $D(k_m)$ defined in (A.8) and associated with modes with non-zero mean (resonant frequencies with zero-mean modes are not displayed here).

Incident plane wave. In a first case, an incident plane wave is considered and the initial conditions read

$$\boldsymbol{U}(\boldsymbol{X}, 0) = \begin{pmatrix} \dfrac{1}{\mu_m} \\ -\dfrac{1}{c_m} \\ 0 \end{pmatrix} F\big((\boldsymbol{X} - \boldsymbol{X}_I) \cdot \boldsymbol{e}_1\big) \tag{39}$$

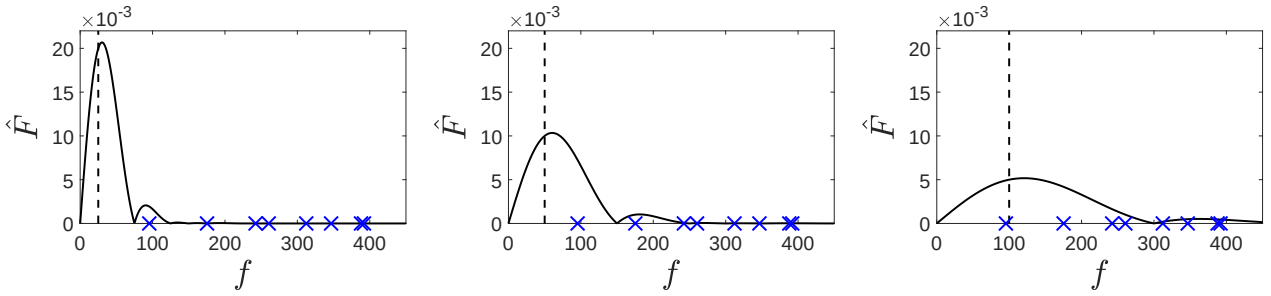

(a) $f_0 = 25\,\text{Hz}$ (b) $f_0 = 50\,\text{Hz}$ (c) $f_0 = 100\,\text{Hz}$

Figure 6: Fourier transform $\hat{F}$ of the *source* function for the three different values f_0 considered (here indicated by the dashed lines). The blue crosses denote the frequencies associated with resonances k_r, see (A.8), of non-zero mean modes.

where the initialization point $\boldsymbol{X}_I = (-2, 0)\,\text{m}$ is chosen such that compactly supported initial conditions (39) do not intersect the enlarged interface. The initial velocity field and profile are displayed in Figure 7 for $f_0 = 100\,\text{Hz}$. The velocity profile is normalized by the maximum homogenized velocity. From now on, it will be the case for all velocity profiles displayed.

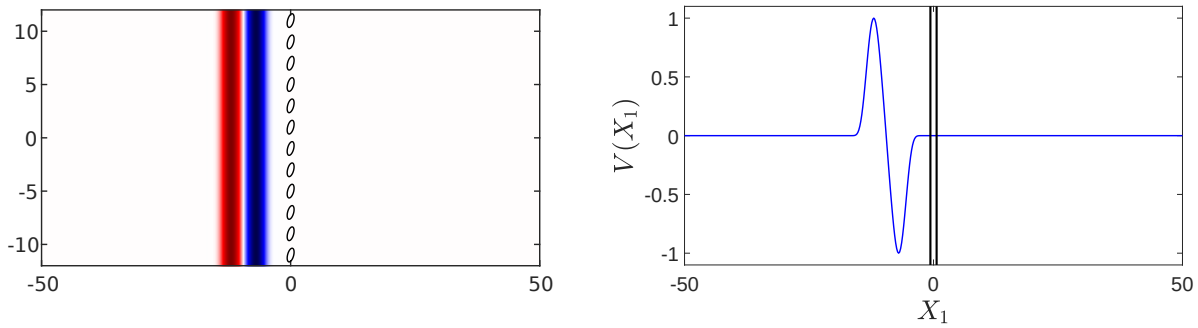

(a) Waveform (b) X_1-profile at $X_2 = -1\,\text{m}$

Figure 7: Velocity field at the time $t = 0$ for the incident plane wave given by (39) with $f_0 = 100\,\text{Hz}$.

Point source. In a second case, we consider a point source located at $\boldsymbol{X}_S = (-35, 0)\,\text{m}$ and such that (1) reads:

$$\begin{cases} \dfrac{\partial \boldsymbol{\Sigma}}{\partial t}(\boldsymbol{X}, t) = \mu_m \boldsymbol{\nabla} V(\boldsymbol{X}, t) \\ \rho_m \dfrac{\partial V}{\partial t}(\boldsymbol{X}, t) = \operatorname{div} \boldsymbol{\Sigma}(\boldsymbol{X}, t) + \rho_m \delta(\boldsymbol{X} - \boldsymbol{X}_s) F(t c_m), \end{cases} \tag{40}$$

with $\delta(\boldsymbol{X} - \boldsymbol{X}_s)$ being a Dirac delta function at $\boldsymbol{X} = \boldsymbol{X}_s$.

3.1.4. Numerical errors

To assess whether the homogenized model provides a satisfying approximation of the original problem in the microstructured configuration, we compare the corresponding numerical solutions. With $\boldsymbol{U}$ and $\boldsymbol{U}^h$ being respectively the exact solution of the original problem in the microstructured configuration and in the homogenized model, we denote by $\mathbf{U}$ and $\mathbf{U}^h$ their numerical approximations.

Defining the global *modeling* error $\varepsilon_T = \|\boldsymbol{U} - \boldsymbol{U}^h\|$, then one has formally by triangular inequality:

$$\varepsilon_T \leq \underbrace{\|\boldsymbol{U} - \mathbf{U}\|}_{\varepsilon_1} + \underbrace{\|\mathbf{U} - \mathbf{U}^h\|}_{\varepsilon_2} + \underbrace{\|\mathbf{U}^h - \boldsymbol{U}^h\|}_{\varepsilon_3}.$$

The term ε_1 is the numerical error associated with the simulation in the microstructured configuration while ε_3 is the one associated with the simulation based on the homogenized model. Both are governed and controlled by the numerical methods employed, see Lombard and Piraux (2004) and Touboul et al. (2020), respectively. In appropriate implementations of the latter, these errors are considered to be negligible compared to ε_2. As a consequence, we consider that the numerical error $\varepsilon_2 = \|\mathbf{U} - \mathbf{U}^h\|$ provides a reliable estimation of the global modeling error ε_T and can be used to measure the validity of the homogenized model.

The homogenized model of Section 2 is derived under Assumptions 1, i.e., with asymptotics being performed in the limit $\eta \to 0$ while it is assumed that $\mu_i/\mu_m = \mathcal{O}(\eta^2)$ to preserve resonances. In practice, we apply this model to a given geometric and material configuration for which the parameters h, μ_i and μ_m are set. The signal (38) is also considered as a *source* term and the latter carries a range of wavelengths λ that are in turn associated with a parameter $\eta(\lambda) = 2\pi h/\lambda = 2\pi h f/c_m$. For Assumptions 1 to hold then one must have both $\eta(\lambda) \ll 1$ and $\eta(\lambda) = \mathcal{O}(\sqrt{\mu_i/\mu_m})$.

As a consequence, the agreement between simulations for the microstructured and the homogenized problems are expected to deteriorate as $\eta(\lambda)$ approaches 1. For the source signal (38) considered, we will only focus on $\eta(f_0)$ but, as seen in Figure 6, the frequency content of this source extends to higher frequencies for which the associated wavelengths may lie beyond the validity domain of Assumptions 1.

3.2. *Incident plane wave at normal incidence*

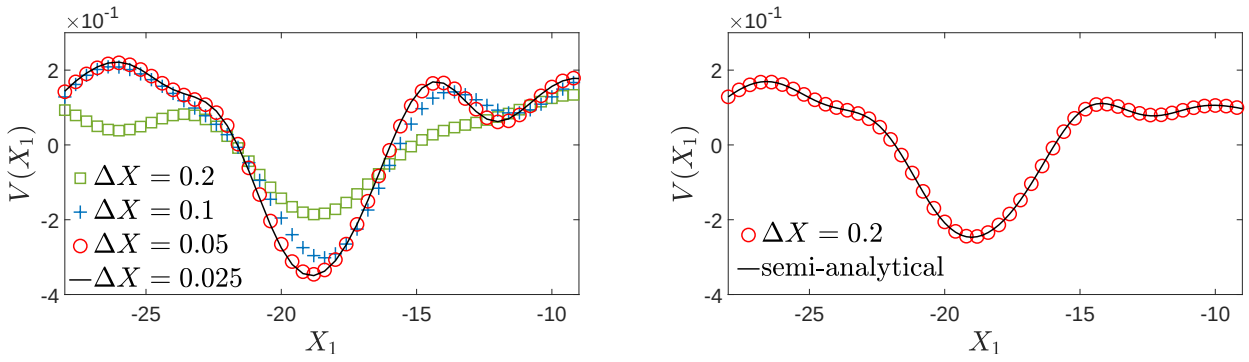

(a) Microstructured configuration: numerical solutions

(b) Homogenized model: numerical and semi-analytical solutions

Figure 8: Velocity profiles for the microstructured configuration and using the homogenized model. The source term is such that $f_0 = 100$ Hz.

In a first example, we consider an incident plane wave at normal incidence, see Section 3.1.3. The velocity profiles of the numerical solutions in the original microstructured configuration are presented in Figure 8a for different mesh sizes. Figure 8b compares the profiles of velocity for the homogenized model, computed either numerically on a grid of mesh size $\Delta X = 0.2$ m or semi-analytically. The latter computation is performed using the method described in Touboul et al. (2020) which relies

on the calculation of the reflexion and transmission coefficients from (A.4). On the one hand, the numerical solution for the microstructured configuration on the fine grid $\Delta X = 0.025\,\mathrm{m}$ is assumed to have converged, see Fig. 8a. On the other hand, a coarse grid $\Delta X = 0.2\,\mathrm{m}$ suffices when using the homogenized model, see Fig. 8b. As an indication of the numerical gain, at $f_0 = 100\,\mathrm{Hz}$, a computational time of 47 seconds for the homogenized model ($\Delta X = 0.2\,\mathrm{m}$ in Fig. 8b) corresponds to a computational time of 4.8 hours for the original microstructured configuration ($\Delta X = 0.025\,\mathrm{m}$ in Fig. 8a). The extra time needed for the original problem is due to the smaller mesh size but also to the smaller time step imposed by the CFL condition for numerical stability. These two mesh sizes will be used in numerical experiments from now on.

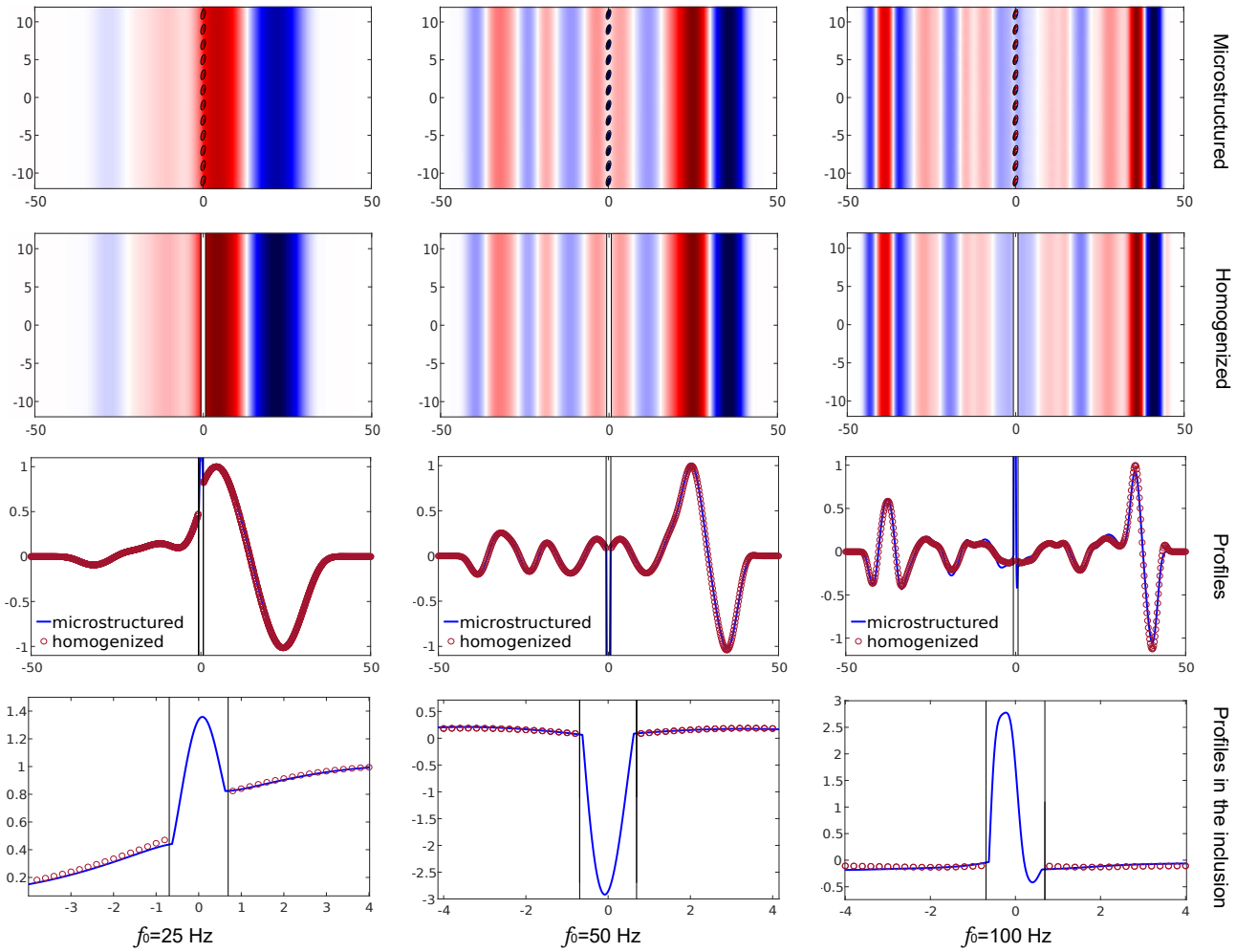

Figure 9: *(Top two rows)* velocity fields for the microstructured configuration and for the homogenized model for an illumination by an incident plane wave at normal incidence. *(Third row)* comparison of the corresponding velocity profiles at $X_2 = -1\,\mathrm{m}$. *(Bottom row)* zoom in the inclusion. *(left)* $f_0 = 25\,\mathrm{Hz}$ and $\eta(f_0) = 0.21$, *(center)* $f_0 = 50\,\mathrm{Hz}$ and $\eta(f_0) = 0.42$, and *(right)* $f_0 = 100\,\mathrm{Hz}$ and $\eta(f_0) = 0.84$.

The velocity fields for the microstructured configuration and for the homogenized model together with their respective profiles along $X_2 = -1\,\mathrm{m}$ are reported in Figure 9 at time $t = 31.7\,\mathrm{ms}$ for $f_0 \in \{25, 50, 100\}\,\mathrm{Hz}$. The corresponding discrepancies between both solutions is measured in the L^2-norm for $X_1 \in [-50; -5]\,\mathrm{m}$ and at $X_2 = -1\,\mathrm{m}$. The relative errors are of about 4%, 7% and

10%, respectively. As expected from the discussion in Section 3.1.4, the solutions agree at low frequency but deviate from one another as the parameter $\eta(f_0)$ increases to 1 and does not conform to the shear modulus ratio. Finally, in Figure 9, it can be observed that the dispersive nature of the material is amplified, in both the microstructured configuration and in the homogenized model, as f_0 increases. This behavior reflects the fact that resonances play an increasing role. At low frequency, the observed wavefield is almost comparable to the case of a non-resonant interface (with non-constrasted inclusions), see Lombard et al. (2017), while at higher frequencies some energy is still radiated by the interface after the incident wave has crossed the latter. In the case $f_0 = 50$ Hz, the velocity in the microstructured and homogenized configuration is recorded from $t = 0$ to $t = 475$ ms at one receiver. This receiver is located on the right of the enlarged interface at $\boldsymbol{X}_T = (X_T, 0)$ m, with $X_T = 10$m. From these data, the Fourier transform of the transmitted velocity $\hat{V}(\boldsymbol{X}_T, f)$ is computed and its logarithm is displayed in Figure 10. The dashed line indicates the logarithm of the Fourier transform of the incident wave. The three logarithms are normalized by the maximum of the logarithm of the homogenized Fourier transform. The figure underlines the fact that the analysis holds for resonances with non null mean value: indeed we have a good agreement between both Fourier transforms around the resonances in $D(k_m)$ (A.8), while the behaviour of the solution is not well described by the homogenized solution around the resonances with null mean value which are not taken into account in $D(k_m)$. However, these missed resonant frequencies also correspond to values of η which are around or higher than 1. Thus, even if the behaviour of the solution is not well described, it is in any case for a range of frequencies that go beyond the low-frequency hypothesis of homogenization. Furthermore, it can also be noticed that these missed resonant frequencies are not solicited a lot by the incident velocity. Therefore, it can be assumed that it doesn't lead to a big deterioration of the results.

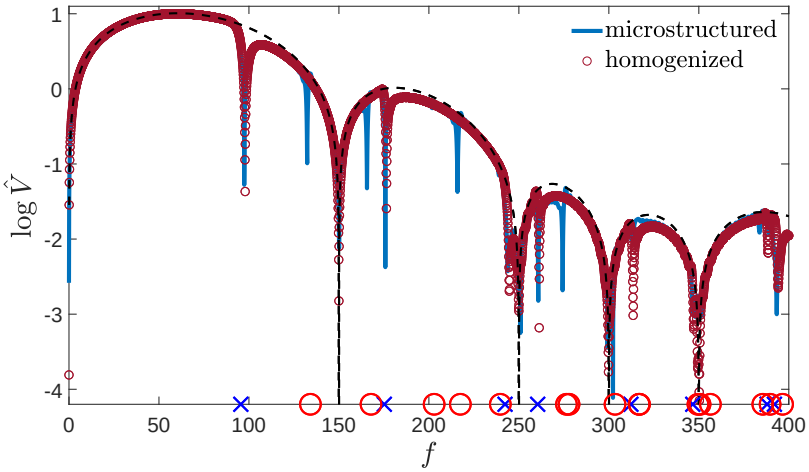

Figure 10: Logarithm of the Fourier transform $\hat{V}(\boldsymbol{X}_T, f)$ for the microstructured and the homogenized configuration. The dashed line indicates the logarithm of the Fourier transform of the incident velocity. The blue crosses denote the resonant frequencies taken into account in $D(k_m)$ (A.8) and the red circles denote the missed resonant frequencies of zero mean modes.

3.3. Point source

In the previous example of Section 3.2, the X_2-invariance of the illumination considered implies that the X_2-derivatives vanish in the effective model (30) so that the associated homogenized coefficients B_2, C_1 and C_2 play no role. As a consequence, to deal with a full 2D configuration, we consider an illumination by the point source described in (40). The physical and numerical parameters are the same as in the previous example. Moreover, the computational domain is defined as

$[-70\text{ m}; 35\text{ m}] \times [-132\text{ m}; 132\text{ m}]$, i.e. it is chosen large enough along the X_2-axis to avoid reflections from the top and bottom boundaries while Perfectly Matched Layers are used in the background domain on the left and right boundaries.

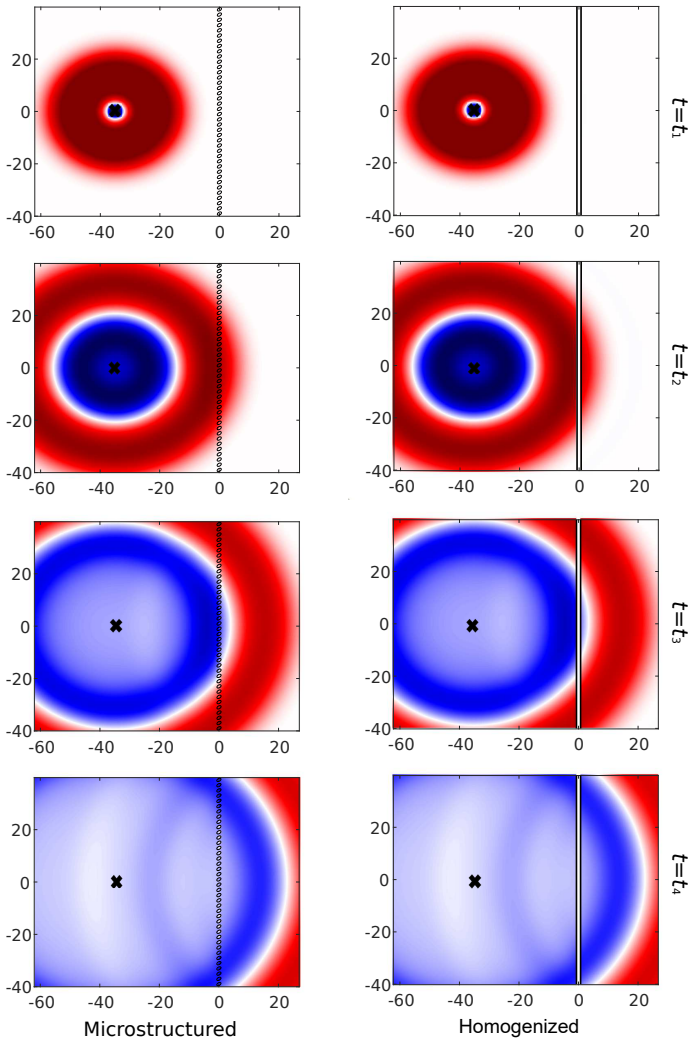

Figure 11: *(Left)* velocity fields for the microstructured configuration and *(right)* for the homogenized model for $f_0 = 25\,\text{Hz}$ (so that $\eta(f_0) = 0.21$) and at different times $t \in \{25.3, 38.0, 50.7, 63.3\}$ ms. A point source is located at $(-35, 0)$ m and symbolized by a black cross. Only a subset of the computational domain is shown here.

The velocity fields for the microstructured configuration and for the homogenized model are displayed at times $t \in \{t_1, t_2, t_3, t_4\} = \{25.3, 38.0, 50.7, 63.3\}$ ms on the figures 11, 12 and 13, which correspond to a source central frequency $f_0 \in \{25, 50, 100\}$ Hz, respectively. The X_1-profiles of both solutions at $X_2 = 1$ m are compared on Figure 14. Quantitatively, the discrepancies between solutions are again measured in the L^2-norm for $X_1 \in [-50\text{ m}\,; -5\text{ m}\,]$ and at $X_2 = 1\,\text{m}$ and the associated relative errors are of 2%, 9% and 13%, respectively, which is of same order than the ones obtained in Section 3.2.

As in the previous example, the agreement between solutions deteriorates as η approaches 1. Figure 14 also displays the velocity profiles zoomed in within a single inclusion in the microstructured configuration. As the frequency increases then shorter wavelengths are *trapped* within the inclusion

and more resonant frequencies featured in (A.8) are solicited, thereby explaining the discrepancies between the two models.

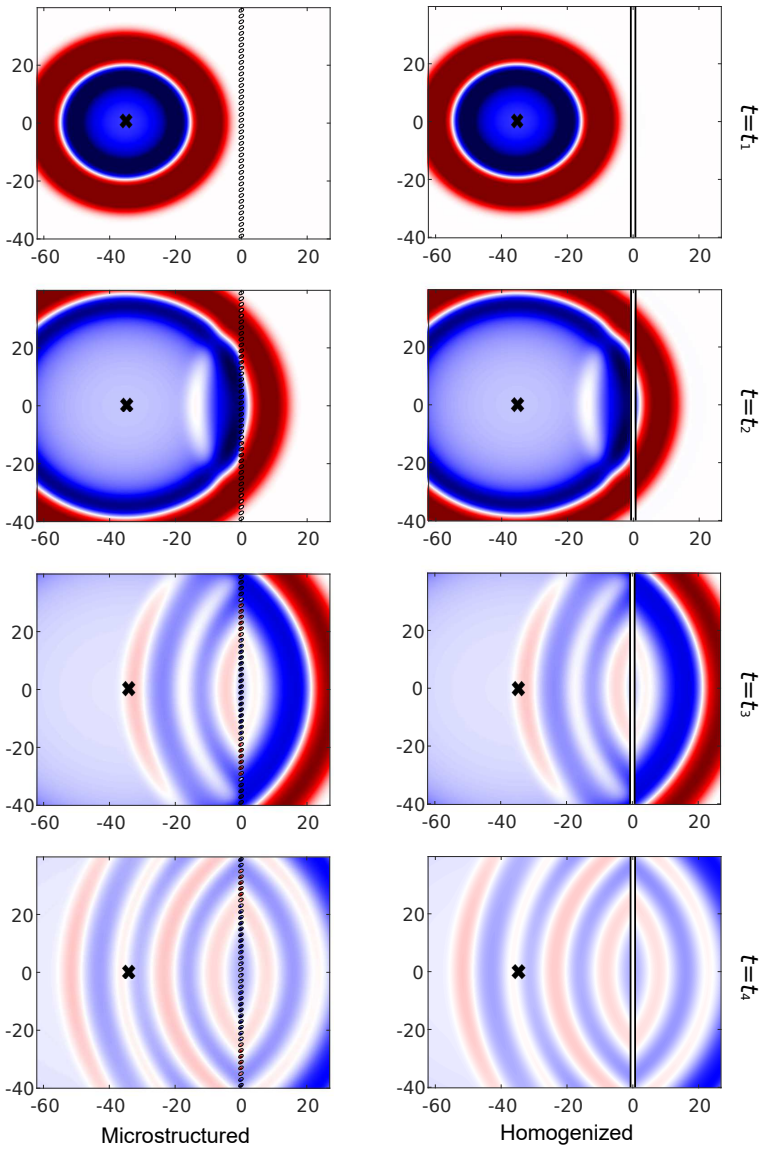

Figure 12: *(Left)* velocity fields for the microstructured configuration and *(right)* for the homogenized model for $f_0 = 50$ Hz (so that $\eta(f_0) = 0.42$) and at different times $t \in \{25.3, 38.0, 50.7, 63.3\}$ ms. A point source is located at $(-35, 0)$ m and symbolized by a black cross. Only a subset of the computational domain is shown here.

4. Conclusion

This study has focused on the propagation of waves across a periodic row of highly-contrasted inclusions, a problem which has been tackled by a homogenization technique. More specifically, the homogenization process has been performed directly in the time domain . The high-contrast between the inclusions and the matrix amounts in a scaling of the shear moduli as η^2 where η is the usual small parameter corresponding to the long-wavelength regime. As a consequence, this produces wavelengths within the inclusions that are comparable to the size of the latter. The specific homogenization process

has led to effective jump conditions that are (i) non-local in time and (ii) apply on the boundaries of an equivalent *enlarged* interface. One notes that no calculation need to be performed anymore within this region. Having the thickness of the effective interface larger than the width of the original microstructured array has been shown to be a sufficient condition to have a stable effective problem. The correspondence of this time-domain effective model with the frequency-dependent jump conditions developed in Pham et al. (2017) has also been established. Finally, numerical examples have been provided to illustrate the model obtained and to compare its solutions with simulations involving the original microstructure. A good agreement has been found at low excitation frequency and it has been discussed how it deteriorates as the frequency increases.

Perspectives include the derivation of an effective model at higher order, as discussed in Felbacq and Bouchitté (2005); Pham et al. (2017), to account for the resonances associated with modes with zero mean, which are missed in the current model. Moreover, it is important to assess to what extent these resonances play a role for the problem under consideration. Another possible future direction concerns the design of meta-interfaces through a dedicated topological optimization process for microstructured periodic arrays in order to reach some objective effective properties, see the approach developed in Cornaggia and Bellis (2020) for bulk metamaterials. For example, this would be of interest for noise reduction by thin resonant meta-interfaces, see Ma et al. (2014); Schwan et al. (2017).

Acknowledgements. We acknowledge the stimulating exchanges promoted by the GDR *MecaWave* of the French Centre National de la Recherche Scientifique. CB, BL and MT are thankful to Rémi Cornaggia for fruitful discussions.

Appendix A. Frequency-domain formulation

With the effective model (30) being derived in the time domain , this section focuses on assessing its equivalence with the frequency-domain formulation obtained in Pham et al. (2017). First, the frequency Fourier transform is defined:

$$\mathscr{F}[f](\boldsymbol{X},\omega) = \hat{f}(\boldsymbol{X},\omega) = \int_{\mathbb{R}} f(\boldsymbol{X},t)e^{-i\omega t}\,\mathrm{d}t,$$

along with the convolution product:

$$[f * g](t) = \int_{\mathbb{R}} f(t-t')g(t)\,\mathrm{d}t'.$$

Due to the final effective jump condition (30), we seek closed-form identity for the field W_i solution of (31). To do so, let us consider the time-domain Green's function associated with the inclusion domain Ω_i and a source point $\boldsymbol{y}_0$, i.e. the field $G : (\boldsymbol{y},t) \mapsto G(\boldsymbol{y},\boldsymbol{y}_0,t)$ that is the fundamental solution of the problem:

$$\begin{cases} \dfrac{\partial^2 G}{\partial t^2}(\boldsymbol{y},\boldsymbol{y}_0,t) - \dfrac{\mu_i}{\rho_i h^2}\Delta_{\boldsymbol{y}} G(\boldsymbol{y},\boldsymbol{y}_0,t) = \delta(\boldsymbol{y}-\boldsymbol{y}_0)\delta(t) & (\boldsymbol{y}\in\Omega_i), \\ G(\boldsymbol{y},\boldsymbol{y}_0,t) = 0 & (\boldsymbol{y}\in\partial\Omega_i), \\ G(\boldsymbol{y},\boldsymbol{y}_0,0) = \dfrac{\partial G}{\partial t}(\boldsymbol{y},\boldsymbol{y}_0,0) = 0 & (\boldsymbol{y}\in\Omega_i). \end{cases}$$

The equations (31) at time $(t-t')$ are multiplied by G taken at time t' and integrated on $\Omega_i \times [0,t]$, which leads to

$$\int_{\Omega_i} \left\{ \left[\frac{\partial^2 W_i}{\partial t^2} * G \right](t) - \frac{\mu_i}{\rho_i h^2} \left[\Delta_{\boldsymbol{y}} W_i * G \right](t) \right\} \mathrm{d}\boldsymbol{y} = 0.$$

Integrating by parts twice, the first term in time and the second term in space, respectively, and using the boundary conditions for W_i and G yields:

$$W_i(\boldsymbol{y}_0, X_2, t) = -\frac{\mu_i}{\rho_i h^2} \left[\left\langle V^h(\cdot, X_2, \cdot) \right\rangle_a * \int_{\partial\Omega_i} \boldsymbol{\nabla}_{\boldsymbol{y}} G(\boldsymbol{y}, \boldsymbol{y}_0, \cdot) \cdot \boldsymbol{n} \, \mathrm{d}\ell \right](t).$$

Going back to (30), we now get formally in the frequency domain:

$$\mathscr{F}\left[\rho_i \int_{\Omega_i} \frac{\partial W_i}{\partial t} \mathrm{d}\boldsymbol{y} \right](\boldsymbol{X}, \omega) = \frac{\rho_i}{\rho_m} \left\langle \operatorname{div} \hat{\boldsymbol{\Sigma}}^h(\cdot, X_2, \omega) \right\rangle_a \int_{\Omega_i} \left\{ -\frac{\mu_i}{\rho_i h^2} \int_{\partial\Omega_i} \boldsymbol{\nabla}_{\boldsymbol{y}_0} \hat{G}(\boldsymbol{y}, \boldsymbol{y}_0, \omega) \cdot \boldsymbol{n} \, \mathrm{d}\ell_0 \right\} \mathrm{d}\boldsymbol{y}, \tag{A.1}$$

where we have used the identity $i\omega\rho_m \hat{V}^h = \operatorname{div} \hat{\boldsymbol{\Sigma}}^h$ and the fact that $\hat{G}(\boldsymbol{y}, \boldsymbol{y}_0, \omega) = \hat{G}(\boldsymbol{y}_0, \boldsymbol{y}, \omega)$. We define the field $\hat{V}_{k_m}$ as

$$\hat{V}_{k_m}(\boldsymbol{y}, \omega) = -\frac{\mu_i}{\rho_i h^2} \int_{\partial\Omega_i} \boldsymbol{\nabla}_{\boldsymbol{y}_0} \hat{G}(\boldsymbol{y}, \boldsymbol{y}_0, \omega) \cdot \boldsymbol{n} \, \mathrm{d}\ell_0. \tag{A.2}$$

Owing to the following relation satisfied by G in the frequency domain

$$\Delta_{\boldsymbol{y}} \hat{G}(\boldsymbol{y}, \boldsymbol{y}_0, \omega) + \frac{\rho_i \mu_m}{\rho_m \mu_0} \hat{G}(\boldsymbol{y}, \boldsymbol{y}_0, \omega) = -\frac{\rho_i h^2}{\mu_i} \delta(\boldsymbol{y} - \boldsymbol{y}_0),$$

then it turns out that $\hat{V}_{k_m}$ is the solution of the following problem:

$$\begin{cases} \Delta_{\boldsymbol{y}} \hat{V}_{k_m}(\boldsymbol{y}, \omega) + \kappa(k_m)^2 \hat{V}_{k_m}(\boldsymbol{y}, \omega) = 0 & (\boldsymbol{y} \in \Omega_i), \\ \hat{V}_{k_m}(\boldsymbol{y}, \omega) = 1 & (\boldsymbol{y} \in \partial\Omega_i), \end{cases} \tag{A.3}$$

where one has defined $\kappa(k_m) = k_m h \sqrt{\dfrac{\rho_i \mu_m}{\rho_m \mu_i}}$.

Therefore, provided that the Fourier transforms are well-defined, the time-domain model developed here is in agreement with the frequency-domain model of Pham et al. (2017), see Equation (44) in the latter:

$$\begin{cases} \left[\!\left[\hat{V}^h \right]\!\right]_a = h \left\{ B \left\langle \dfrac{\partial \hat{V}^h}{\partial X_1} \right\rangle_a + B_2 \left\langle \dfrac{\partial \hat{V}^h}{\partial X_2} \right\rangle_a \right\} & (X_2 \in \mathbb{R}) \\ \left[\!\left[\hat{\Sigma}_1^h \right]\!\right]_a = h \left\{ S \left\langle \dfrac{\partial \hat{\Sigma}_1^h}{\partial X_1} \right\rangle_a + C_1 \left\langle \dfrac{\partial \hat{\Sigma}_1^h}{\partial X_2} \right\rangle_a + C_2 \left\langle \dfrac{\partial \hat{\Sigma}_2^h}{\partial X_2} \right\rangle_a + D(k_m) \left\langle \operatorname{div} \hat{\boldsymbol{\Sigma}}^h \right\rangle_a \right\} & (X_2 \in \mathbb{R}), \end{cases} \tag{A.4}$$

where, due to (A.1) and (A.2), one has:

$$D(k_m) = \frac{\rho_i}{\rho_m} \int_{\Omega_i} \hat{V}_{k_m}(\boldsymbol{y}) \, \mathrm{d}\boldsymbol{y}. \tag{A.5}$$

Consequently, the agreement of the time-domain effective model with the frequency-dependent jump conditions is established. However, thanks to the time-domain formulation, we were able to perform an energy analysis and provide a sufficient condition for the effective model to be stable.

As shown in Pham et al. (2017), the solution $\hat{V}_{k_m}$ to (A.3) can be found as an expansion onto the function basis of the eigensystem $(\lambda_r, P_r)_{r\geq 1}$ that is associated with the following self-adjoint eigenvalue problem within the inclusion:

$$\begin{cases} \Delta_{\boldsymbol{y}} P_r(\boldsymbol{y}) + \lambda_r P_r(\boldsymbol{y}) = 0 & \text{in } \Omega_i, \\ P_r(\boldsymbol{y}) = 0 & \text{on } \partial\Omega_i. \end{cases} \tag{A.6}$$

In particular, let us define the resonant frequencies $\{k_r\}_{r\geq 1}$ and the real-valued coefficients $\{\alpha_r\}_{r\geq 0}$ as follows

$$\alpha_0 = \int_{\Omega_i} \mathrm{d}\boldsymbol{y} \qquad \alpha_r = \int_{\Omega_i} P_r(\boldsymbol{y})\,\mathrm{d}\boldsymbol{y} \qquad \text{and} \qquad k_r = \frac{1}{h}\sqrt{\frac{\rho_m \mu_i}{\rho_i \mu_m}\lambda_r}. \tag{A.7}$$

Then the term $D(k_m)$ in (A.5) can be recast as the following *infinite* series:

$$D(k_m) = \frac{\rho_i}{\rho_m}\left\{\alpha_0 - \sum_{r\geq 1} \alpha_r^2 \frac{k_m^2}{k_m^2 - k_r^2}\right\}. \tag{A.8}$$

Note that, due to the expression of α_r in (A.7), the eigenmodes P_r that have zero mean value do not contribute to the effective model obtained. Moreover, this expression of $D(k_m)$ will be used later on in the numerical method chosen to handle this non-local in time jump conditions.

Appendix B. Positivity of the parameter B

We seek a lower bound for the parameter B that is defined by (29) and (15). It is useful for the energy analysis of Section 2.2, see Equation (35). To do so, we consider the variational formulation (37) that is satisfied by the field $\Phi^{(1)}$. Moreover, let us define the following quadratic functional:

$$\mathcal{L}\big(\tilde{\Phi}\big) = \int_{\Omega\backslash\Omega_i} \big[\frac{1}{2}\boldsymbol{\nabla}_{\boldsymbol{y}}\tilde{\Phi}(\boldsymbol{y}) + \boldsymbol{e}_1\big] \cdot \boldsymbol{\nabla}_{\boldsymbol{y}}\tilde{\Phi}(\boldsymbol{y})\,\mathrm{d}\boldsymbol{y} - \lim_{y_1\to+\infty} \int_{-1/2}^{1/2} \big[\tilde{\Phi}(y_1, y_2) - \tilde{\Phi}(-y_1, y_2)\big]\mathrm{d}y_2.$$

Then, owing to (37), the field $\Phi^{(1)}$ minimizes $\mathcal{L}$ on $\mathcal{H}^{\text{per}}_{0,1}(\Omega\backslash\Omega_i)$ and one has

$$\mathcal{L}\big(\Phi^{(1)}\big) = -\frac{B_1}{2} + \frac{1}{2}\int_{\Omega\backslash\Omega_i} \boldsymbol{\nabla}_{\boldsymbol{y}}\Phi^{(1)} \cdot \boldsymbol{e}_1\,\mathrm{d}\boldsymbol{y}. \tag{B.1}$$

To have an explicit expression of the second term, we multiply the cell problem (16) by the function y_1 and we integrate in the bounded domain $\Omega^b\backslash\Omega_i$, i.e.

$$\int_{\Omega^b\backslash\Omega_i} \Delta_{\boldsymbol{y}}(\Phi^{(1)} + y_1) y_1\,\mathrm{d}\boldsymbol{y} = 0.$$

By integration by parts and due to the periodicity and boundary conditions for $\Phi^{(1)}$, this equation leads to

$$\int_{-1/2}^{1/2} \big[\boldsymbol{\nabla}_{\boldsymbol{y}}\Phi^{(1)}(-y_1^b, y_2) + \boldsymbol{\nabla}_{\boldsymbol{y}}\Phi^{(1)}(y_1^b, y_2)\big] \cdot y_1^b \boldsymbol{e}_1\,\mathrm{d}y_2 + 2y_1^b - \int_{\Omega^b\backslash\Omega_i} \boldsymbol{\nabla}_{\boldsymbol{y}}\Phi^{(1)} \cdot \boldsymbol{e}_1\,\mathrm{d}\boldsymbol{y} - \int_{\Omega^b\backslash\Omega_i} \mathrm{d}\boldsymbol{y} = 0.$$

Given that the last integral is equal to $(2y_1^b - e\varphi/h)$, then considering the previous identity in the limit $y_1^b \to +\infty$ entails

$$\int_{\Omega\backslash\Omega_i} \boldsymbol{\nabla}_{\boldsymbol{y}} \Phi^{(1)} \cdot \boldsymbol{e}_1 \, \mathrm{d}\boldsymbol{y} = \frac{e\varphi}{h},$$

and thus, from (B.1), one gets

$$\mathcal{L}\big(\Phi^{(1)}\big) = -\frac{B_1}{2} + \frac{e\varphi}{2h}.$$

As a consequence and due to the minimization principle for $\mathcal{L}$, one obtains the following lower bound for B_1:

$$B_1 \geq \frac{e\varphi}{h} - 2\mathcal{L}\big(\tilde{\Phi}\big) \qquad \forall \tilde{\Phi} \in \mathcal{H}^{\text{per}}_{0,1}(\Omega\backslash\Omega_i). \tag{B.2}$$

To have an explicit bound, we define $\tilde{\Phi} \in \mathcal{H}^{\text{per}}_{0,1}(\Omega\backslash\Omega_i)$ as the piecewise linear function:

$$\tilde{\Phi}(\boldsymbol{y}) = 2\tilde{\beta}h\frac{y_1}{e} \quad \text{if } 0 \leq |y_1| \leq \frac{e}{2h} \quad \text{and} \quad \tilde{\Phi}(\boldsymbol{y}) = \tilde{\beta}\,\mathrm{sign}(y_1) \quad \text{if } |y_1| \geq \frac{e}{2h}$$

with $\tilde{\beta}$ a constant, from which one gets:

$$\mathcal{L}\big(\tilde{\Phi}\big) = 2\frac{h}{e}(1-\varphi)\tilde{\beta}^2 - 2\tilde{\beta}\varphi.$$

As a quadratic function of $\tilde{\beta}$, then $\mathcal{L}\big(\tilde{\Phi}\big)$ reaches a minimum for $\tilde{\beta} = \frac{e\varphi}{2h(1-\varphi)}$, which inserted in (B.2) yields:

$$B_1 \geq \frac{e\varphi}{h} + \frac{e\varphi^2}{h(1-\varphi)}.$$

To conclude, using (29), one finally obtains the following positive lower bound for B:

$$B \geq \frac{a}{h} + \frac{e\varphi}{h} + \frac{e\varphi^2}{h(1-\varphi)} \geq 0.$$

Appendix C. Positivity of the term $(S - C_2)$

We seek a lower bound for the term $(S - C_2)$ that is featured in (35) and is defined by (29) and (23). Let us introduce $\boldsymbol{\Psi}^{(2)} = (\boldsymbol{\nabla}_{\boldsymbol{y}}\Phi^{(2)} + \boldsymbol{e}_2)$. Owing to the definition of the field $\Phi^{(2)}$ as the solution to (16) and based on the definition of the functional space $\mathcal{H}^{\text{per}}_{0,2}(\Omega\backslash\Omega_i)$ we consider in addition the following admissibility space:

$$\mathcal{W}^{\text{per}}(\Omega\backslash\Omega_i) = \Big\{(\boldsymbol{f} - \boldsymbol{e}_2) \in L^2_{\text{loc}}(\Omega\backslash\Omega_i) \text{ with } \boldsymbol{f}(y_1, y_2 + 1) = \boldsymbol{f}(y_1, y_2) \text{ for all } \boldsymbol{y} \in \Omega\backslash\Omega_i$$
$$\text{and such that } \operatorname{div}_{\boldsymbol{y}} \boldsymbol{f} = 0 \text{ in } \Omega\backslash\Omega_i,\ \boldsymbol{f}\cdot\boldsymbol{n} = 0 \text{ on } \partial\Omega_i \text{ and } \lim_{y_1 \to \pm\infty} \boldsymbol{f} = \boldsymbol{e}_2\Big\},$$

so that $\boldsymbol{\Psi}^{(2)} \in \mathcal{W}^{\text{per}}(\Omega\backslash\Omega_i)$. We also introduce for any $\tilde{\boldsymbol{\Psi}} \in \mathcal{W}^{\text{per}}(\Omega\backslash\Omega_i)$ the following functional:

$$\mathcal{M}\big(\tilde{\boldsymbol{\Psi}}\big) = \frac{1}{2}\int_{\Omega\backslash\Omega_i} \big|\tilde{\boldsymbol{\Psi}} - \boldsymbol{e}_2\big|^2 \, \mathrm{d}\boldsymbol{y}.$$

Upon noticing that for any admissible field $\tilde{\boldsymbol{\Psi}}$ the derivative of $\mathcal{M}$ in $\mathcal{W}^{\text{per}}(\Omega\backslash\Omega_i)$ satisfies

$$\mathcal{M}'\big[\boldsymbol{\Psi}^{(2)}\big]\tilde{\boldsymbol{\Psi}} = \int_{\Omega\backslash\Omega_i} \boldsymbol{\nabla}_{\boldsymbol{y}}\Phi^{(2)} \cdot \tilde{\boldsymbol{\Psi}} \, \mathrm{d}\boldsymbol{y} = \int_{\partial(\Omega\backslash\Omega_i)} \Phi^{(2)}\tilde{\boldsymbol{\Psi}}\cdot\boldsymbol{n} \, \mathrm{d}\boldsymbol{y} - \int_{\Omega\backslash\Omega_i} \Phi^{(2)} \operatorname{div}_{\boldsymbol{y}} \tilde{\boldsymbol{\Psi}} \, \mathrm{d}\boldsymbol{y} = 0,$$

then $\boldsymbol{\Psi}^{(2)}$ minimizes the quadratic functional $\mathcal{M}$. Moreover, from the cell problem (16) one has

$$\int_{\Omega\backslash\Omega_i} \Delta_{\boldsymbol{y}}(\Phi^{(2)} + y_2)\Phi^{(2)}\,\mathrm{d}\boldsymbol{y} = 0.$$

By integration by parts and due to the periodicity and boundary conditions for $\Phi^{(2)}$ and its derivatives, this leads to

$$C_2 = \int_{\Omega\backslash\Omega_i} \left|\boldsymbol{\nabla}_{\boldsymbol{y}}\Phi^{(2)}\right|^2 \mathrm{d}\boldsymbol{y} = 2\mathcal{M}\big(\boldsymbol{\Psi}^{(2)}\big).$$

As a consequence, we obtain that $C_2 \leq 2\mathcal{M}\big(\tilde{\boldsymbol{\Psi}}\big)$ for all $\tilde{\boldsymbol{\Psi}} \in \mathcal{W}^{\text{per}}(\Omega\backslash\Omega_i)$. Finally, we define $\tilde{\boldsymbol{\Psi}}$ as

$$\tilde{\boldsymbol{\Psi}}(\boldsymbol{y}) = \boldsymbol{0} \quad \text{if } 0 \leq |y_1| < \frac{e}{2h} \quad \text{and} \quad \tilde{\boldsymbol{\Psi}}(\boldsymbol{y}) = \boldsymbol{e}_2 \quad \text{if } |y_1| \geq \frac{e}{2h}$$

from which one gets $\mathcal{M}(\tilde{\boldsymbol{\Psi}}) = e(1-\varphi)/(2h)$. From the minimization principle, we finally obtain the following lower bound $(S - C_2) \geq (a-e)/h$, which proves that $(S - C_2) \geq 0$ if $a \geq e$.

Auriault, J.-L., Boutin, C., nov 2012. Long wavelength inner-resonance cut-off frequencies in elastic composite materials. International Journal of Solids and Structures 49 (23-24), 3269–3281.

Bensoussan, A., Lions, J.-L., Papanicolaou, G., 2011. Asymptotic analysis for periodic structures. AMS Chelsea Publishing.

Bonnet-Bendhia, A., Drissi, D., Gmati, N., 2004. Simulation of muffler's transmission losses by a homogenized finite element method. Journal of Computational Acoustics 12 (3), 447âĂŞ474.

Cornaggia, R., Bellis, C., 2020. Tuning effective dynamical properties of periodic media by fft-accelerated topological optimization. International Journal for Numerical Methods in Engineering.

David, M., Pideri, C., Marigo, J.-J., 2012. Homogenized interface model describing inhomogeneities located on a surface. Journal of Elasticity 109 (2), 153âĂŞ187.

Delourme, B., 2010. ModÃĺles asymptotiques des interfaces fines et pÃľriodiques en ÃľlectromagnÃľtisme. PhD thesis - UniversitÃľ Pierre et Marie Curie - Paris VI.

Felbacq, D., Bouchitté, G., may 2005. Theory of mesoscopic magnetism in photonic crystals. Physical Review Letters 94 (18).

Lombard, B., Maurel, A., Marigo, J.-J., 2017. Numerical modeling of the acoustic wave propagation across an homogenized rigid microstructure in the time domain. Journal of Computational Physics 335, 558–577.

Lombard, B., Piraux, J., mar 2004. Numerical treatment of two-dimensional interfaces for acoustic and elastic waves. Journal of Computational Physics 195 (1), 90–116.

Lombard, B., Piraux, J., Gélis, C., Virieux, J., jan 2008. Free and smooth boundaries in 2-D finite-difference schemes for transient elastic waves. Geophysical Journal International 172 (1), 252–261.

Lorcher, F., Munz, C.-D., nov 2006. Lax-wendroff-type schemes of arbitrary order in several space dimensions. IMA Journal of Numerical Analysis 27 (3), 593–615.

Ma, G., Yang, M., Xiao, S., Yang, Z., Sheng, P., jun 2014. Acoustic metasurface with hybrid resonances. Nature Materials 13 (9), 873–878.

Marigo, J.-J., Maurel, A., 2016. Homogenization models for thin rigid structured surfaces and films. The Journal of the Acoustical Society of America 140 (1), 260–273.

Marigo, J.-J., Maurel, A., Pham, K., Sbitti, A., 2017. Effective dynamic properites of a row of elastic inclusions: The case of scalar shear waves. Journal of Elasticity 128 (2), 265–289.

Marigo, J.-J., Pideri, C., 2011. The effective behaviour of elastic bodies containing microcracks or microholes localized on a surface. International Journal of Damage Mechanics, SAGE Publications 20, 1151–1177.

Maurel, A., Mercier, J.-F., Pham, K., Marigo, J.-J., Ourir, A., apr 2019a. Enhanced resonance of sparse arrays of helmholtz resonators—application to perfect absorption. The Journal of the Acoustical Society of America 145 (4), 2552–2560.

Maurel, A., Pham, K., Marigo, J.-J., aug 2019b. Homogenization of thin 3d periodic structures in the time domainâĂŞeffective boundary and jump conditions. In: Romero-García, V., Hladky-Hennion, A.-C. (Eds.), Fundamentals and Applications of Acoustic Metamaterials. Wiley.

Pham, K., Maurel, A., Marigo, J.-J., 2017. Two scale homogenization of a row of locally resonant inclusions - the case of shear waves. Journal of the Mechanics and Physics of Solids 106, 80–94.

Sanchez-Hubert, J., Sanchez-Palencia, E., 1992. Introduction aux mÃľthodes asymptotiques et Ãă l'homogÃľnÃľisation. Collection MathÃľmatiques AppliquÃľes pour la MaÃőtrise.

Schwan, L., Umnova, O., Boutin, C., jul 2017. Sound absorption and reflection from a resonant metasurface: Homogenisation model with experimental validation. Wave Motion 72, 154–172.

Schwartzkopff, T., Dumbser, M., Munz, C.-D., jul 2004. Fast high order ADER schemes for linear hyperbolic equations. Journal of Computational Physics 197 (2), 532–539.

Touboul, M., Lombard, B., Bellis, C., aug 2020. Time-domain simulation of wave propagation across resonant meta-interfaces. Journal of Computational Physics 414, 109474.

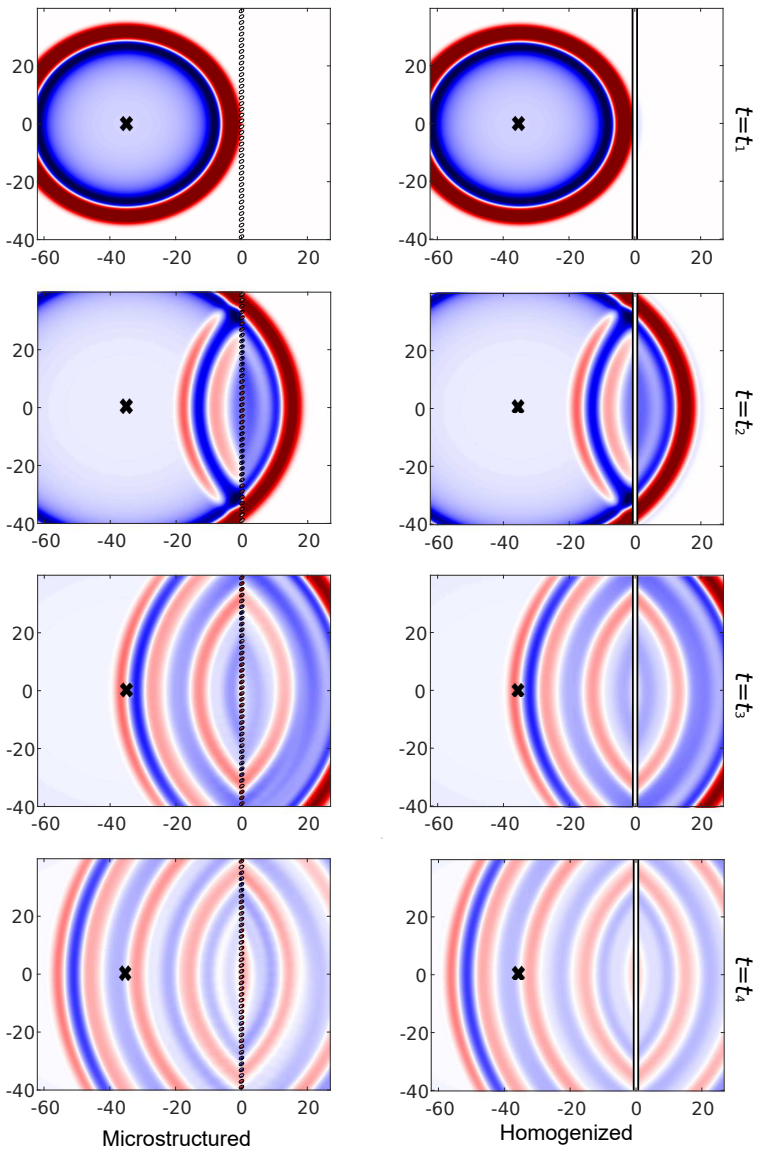

Figure 13: *(Left)* velocity fields for the microstructured configuration and *(right)* for the homogenized model for $f_0 = 100$ Hz (so that $\eta(f_0) = 0.84$) and at different times $t \in \{25.3, 38.0, 50.7, 63.3\}$ ms. A point source is located at $(-35, 0)$ m and symbolized by a black cross. Only a subset of the computational domain is shown here.

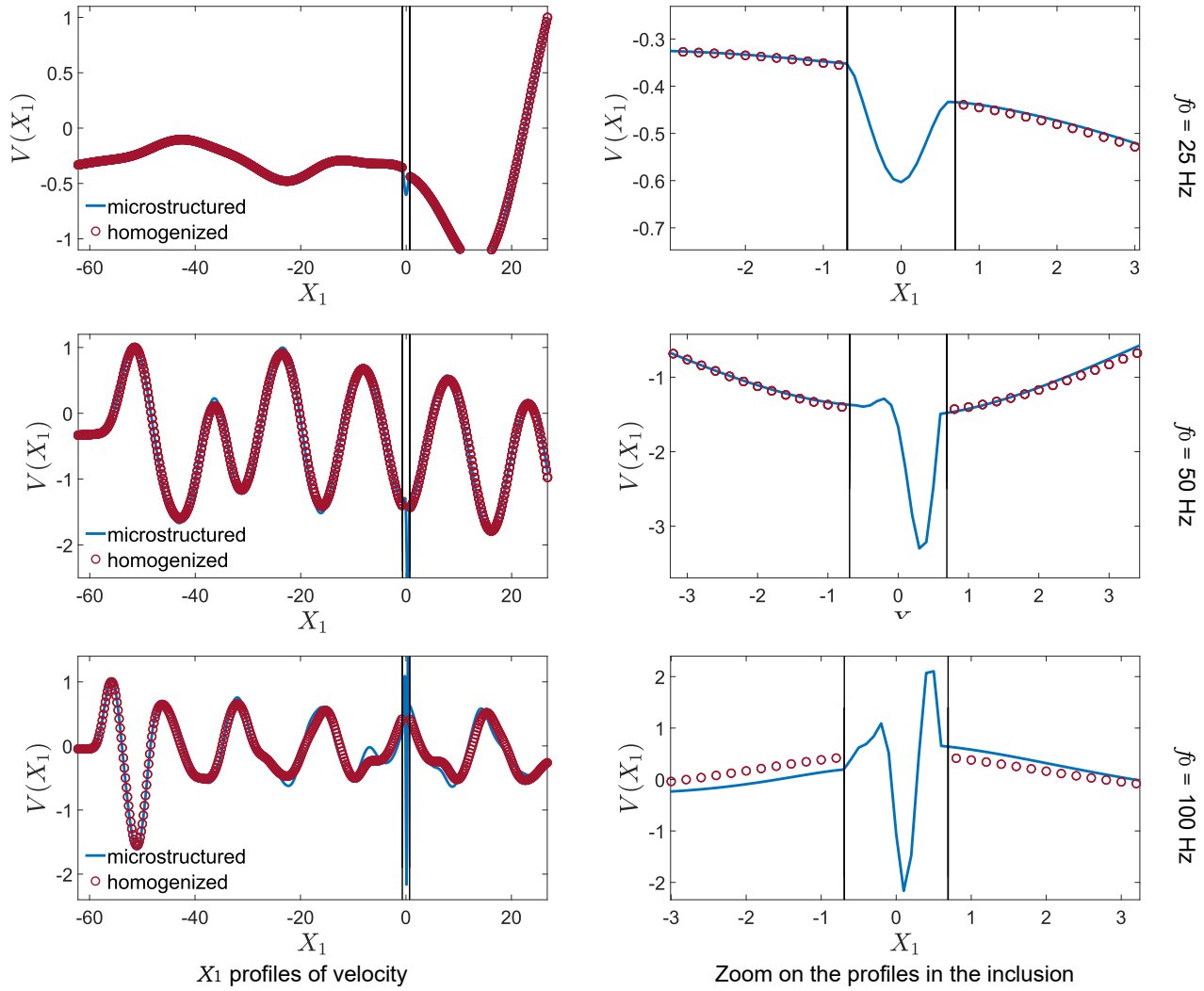

Figure 14: Comparisons of the velocity profiles for the microstructured configuration and the homogenized model at $X_2 = 1$ m. *(Left)* subset of the computational domain, and *(right)* zoom in the inclusion region. From top to bottom rows: $f_0 \in \{25, 50, 100\}$ Hz, respectively, which corresponds to $\eta(f_0) \in \{0.21, 0.42, 0.84\}$.